

Printed October 29, 2018

A Comprehensive Study of the L1551 IRS 5 Binary System

Mayra Osorio¹, Paola D'Alessio², James Muzerolle³, Nuria Calvet¹, Lee Hartmann¹

ABSTRACT

We model the Class I source L1551 IRS 5, adopting a flattened infalling envelope surrounding a binary disk system and a circumbinary disk. With our composite model, we calculate self-consistently the spectral energy distribution of each component of the L1551 IRS 5 system, using additional constraints from recent observations by ISO, the water ice feature from observations with SpeX, the SCUBA extended spatial brightness distribution at sub-mm wavelengths, and the VLA spatial intensity distributions at 7 mm of the binary disks. We analyze the sensitivity of our results to the various parameters involved. Our results show that a flattened envelope collapse model is required to explain simultaneously the large scale fluxes and the water ice and silicate features. On the other hand, we find that the circumstellar disks are optically thick in the millimeter range and are inclined so that their outer parts hide the emission along the line of sight from their inner parts. We also find that these disks have lower mass accretion rates than the infall rate of the envelope.

Subject headings: Physical data and processes: binary, disks — stars: circumstellar matter, formation — ISM: individual (L1551 IRS 5)

1. INTRODUCTION

L1551 IRS 5 in Taurus (distance 140 pc; Kenyon, Dobrzycka & Hartmann 1994) is one of the most extensively studied young stellar objects (YSOs). It is the prototypical

¹Harvard-Smithsonian Center for Astrophysics, 60 Garden St., Cambridge, MA 02138, USA; mosorio@cfa.harvard.edu, p.dalessio@astro.unam.mx, jamesm@as.arizona.edu, ncalvet@cfa.harvard.edu, hartmann@cfa.harvard.edu

²Instituto de Astronomía, UNAM, Ap. Postal 70-264, Cd. Universitaria, 04510 México D.F., México

³Steward Observatory, University of Arizona, 933 North Cherry Avenue, Room N204, Tucson, AZ 85721-0065

embedded YSO (Strom, Strom, & Vrba 1976) with a massive molecular outflow (Snell, Loren & Plambeck et al. 1980). Adams, Lada, & Shu (1987) identified it as a protostellar (Class I) source with an estimated infall rate for its envelope of $\sim 10^{-5} M_{\odot} \text{ yr}^{-1}$. The near-infrared spectrum exhibits first-overtone absorption in CO, suggesting that IRS 5 is an FU Ori object (Carr, Harvey, & Lester 1987), consistent with an analysis of the optical spectrum observed in scattered light (Mundt et al. 1985 and Stocke et al. 1988). Given the wide variety of observational constraints available, L1551 IRS 5 is clearly an ideal system for investigating the circumstellar environment that surrounds protostars and to understand its implications for the general process of star formation.

The spectral energy distribution (SED) of dust thermal emission in L1551 IRS 5 and spatial intensity profile at several wavelengths have been modeled previously by several authors (Adams, Lada, & Shu 1987; Butner et al. 1991; Kenyon, Calvet & Hartmann 1993, hereafter KCH93; Men’shchikov & Henning 1997; White et al. 2000). Many of the models developed so far predict SEDs with silicate absorption features much deeper than that revealed by recent observations with the Infrared Space Observatory (ISO) and adopt outer envelopes smaller than indicated by sub-mm SCUBA observations (Chandler & Richer 2000). Some models assume simple power-law density distributions for the circumstellar envelope without requiring physical self-consistency. In addition, in most of the models, L1551 IRS 5 is considered as a single-star system, while high-resolution interferometric observations (Rodríguez et al. 1998) indicate that IRS 5 is a binary.

In this work, we present a physically self-consistent model to investigate the circumstellar material in L1551 IRS 5 on different scales. We assume flattened envelope models (Hartmann et al. 1994; Hartmann, Calvet & Boss 1996, HCB96) for which we solve the transfer of radiation following the methods described by KCH93 and HCB96. We further adopt viscous accretion disks that take into account the irradiation by the envelope such as those described by D’Alessio, Calvet & Hartmann (1997, DCH97). With this composite model, we self-consistently calculate the overall SED and spectral features, the sub-mm spatial intensity profile, the SEDs of the inner disks, and compare with observations to constrain the envelope and disk parameters.

This paper is organized as follows. In §2 we present a description of the L1551 IRS 5 system, with a summary of the observations used in our modeling efforts. In §3 we report spectra at 2-5 microns which constrain disk properties and ice absorption. In §4 we discuss the main assumptions of our modeling. In §5 we present our results and in §6 we discuss them. Finally, in §7 we present a summary and conclusions.

2. THE L1551 IRS 5 SYSTEM

The complexity of the inner regions of IRS 5 has been increasingly recognized in recent years. The possibility of the central source being a binary system was first suggested by Bieging & Cohen (1985) from cm-wave observations and Looney, Mundy, & Welch (1997) from mm-wave data. Detailed interferometric observations at 7 mm clearly show dust emission in two compact elongated structures with diameters ~ 20 AU, which presumably are the circumstellar disks of a binary system (Rodríguez et al. 1998). Each disk may have its own ionized jet (Rodríguez et al. 1998; Fridlund & Liseau 1998).

On somewhat larger scales, mm-wave observations suggest an elongated structure with scales of ~ 100 -400 AU (Keene & Masson et al. 1990; Lay et al. 1994; Looney et al. 1997). This structure may correspond to a circumbinary ring or disk, (Looney et al. 1997), as in the case of GG Tau (Dutrey, Guilloteau & Simon 1994). A structure with size in the range of $400 < R_{\text{ext}} \lesssim 1000$ AU has been inferred from millimeter and submillimeter continuum observations (Ladd et al. 1995, Hogerheijde et al. 1997), but it is difficult to know if this structure corresponds to the circumbinary disk or to the inner part of the extended envelope.

Sub-mm images of broad dynamic range obtained with SCUBA (Chandler & Richer 2000) as well as millimeter continuum observations with IRAM (Motte & André 2001) reveal dust thermal emission at large scales extending ~ 10000 AU in L1551 IRS 5. The large-scale structure of the envelope is flattened (Saito et al. 1996; Momose et al. 1998; Fridlund et al 2002). Observations carried out by Ladd et al. (1995) at submillimeter continuum reveal a large-scale cross-shaped pattern with size ~ 1400 AU which may be caused by the outflow carving out a section of the circumstellar material, consistent with the observation of scattered light in the outflow lobe (Strom et al. 1976; Stocke et al. 1988).

In summary, the L1551 IRS 5 system appears to contain two protostars, each surrounded by a circumstellar disk, both encircled by a circumbinary disk, and all disks surrounded by an extended infalling flattened envelope. Our complex model contains all these components; we need therefore to constrain parameters using the available data over a wide range of wavelengths, as outlined above. Table 1 lists the long wavelength data ($\lambda > 300 \mu\text{m}$) we aim to model, compiled from the literature, with references indicated. Column 3 gives the angular resolution of the observations, and column 5 indicates the estimated radius of the observed structure in the corresponding reference. Fluxes at $\lambda < 300 \mu\text{m}$ are taken from the compilation of KCH93. We also use spectroscopic observations carried out by the ISO Long and Short Wavelength spectrometers (LWS, SWS) toward IRS 5 (White et al. 2000), as well as our scaled data from SpeX (§3).

3. NEAR-IR OBSERVATIONS

We obtained a near-infrared spectrum of L1551 IRS 5 with SpeX (Rayner et al. 1998) at the IRTF, on Jan. 5, 2001 (Muzerolle et al. 2002, in preparation). Since the spectrograph contains a cross-disperser, one can obtain a spectrum across several bandpasses simultaneously; our spectrum has a wavelength range of 2.1 - 4.8 microns, spanning K, L, and a portion of M. The spectral resolution was $R \sim 2000$. The data were taken in a series of 10 “ABBA” offsets, with 2 coadded 10-second exposures at each position. The spectrum was reduced in part using the facility IDL program “Spextool”. Wavelength calibration was done via an arc lamp spectrum and the sky emission lines, and is accurate to about 0.001 microns. In order to remove telluric absorption lines, a spectrum of a solar-type star was taken near in time and airmass to the L1551 observation. After dividing by the standard spectrum, the solar spectrum was used to remove residual features due to photospheric absorption lines in the standard. The observed spectrum is plotted in Figure 1. The broad water ice feature at $\lambda \sim 3.1\mu\text{m}$ and the first overtone bands of CO at $\lambda \sim 2.3\mu\text{m}$ are apparent. Also noticeable is the CO solid feature at $\lambda \sim 4.7\mu\text{m}$.

4. THE MODEL

As suggested by the observations (§2), our model includes two circumstellar disks, a circumbinary disk, and a flattened envelope. A sketch of the model is shown in Figure 2. We describe in this section the assumptions we use to model each component of the system.

4.1. Envelope

We adopt the analytic model for the flattened density distribution resulting from the gravitational collapse of a sheet initially in hydrostatic equilibrium developed by Hartmann et al. (1994) and HCB96, hereafter called η models. These models produce envelopes with a flat density structure at large scales, consistent with observations (§2). The parameters that describe the properties of the envelope models are η , which is a measure of its asphericity ($\eta = R_{\text{out}}/H$, where R_{out} is the outer radius of the envelope and H is the scale height; see HCB96); ρ_1 , the density that the infalling envelope would have at 1 AU if there were no rotation and flattening (KCH93); and R_c , the centrifugal radius (Cassen & Moosman 1981; Terebey, Shu, & Cassen 1984), which is the largest radius on the equatorial plane that receives the infalling material.

The temperature structure of the envelope is calculated from the condition of radiative

equilibrium, assuming a single central source. The spherically symmetric temperature is calculated using an angle-averaged density, as in KCH93. The luminosity of the central source is taken as the sum of the luminosities of the binary circumstellar disks, which are much brighter than their central stars (§5.3). The spectrum of the central source impinging on the inner radius of the envelope, taken as the dust destruction radius, is that of a disk with luminosity equal to the total luminosity. The temperature at the dust destruction radius is assumed to be ~ 1200 K, corresponding to the sublimation temperature of silicates in a low density environment (D’Alessio 1996). Finally, the monochromatic emergent specific intensity is calculated by solving the transfer equation along rays that pierce the envelope, using the angle-dependent density distribution, as in KCH93 and HCB96. The source function is calculated with a mean intensity which includes the direct radiation from the central source, and the diffuse field from the spherically symmetric calculation (cf. Calvet et al. 1994). The monochromatic emergent flux is obtained by direct spatial integration of the intensity.

We assume that dust in the envelope has the standard grain-size distribution $n(a) \propto a^{-3.5}$ of the interstellar medium, with a minimum grain radius $a_{min}=0.005 \mu\text{m}$ and a maximum radius $a_{max}=0.3 \mu\text{m}$. We use a dust mixture with olivine, organics, troilite and water ice as it is suggested by Pollack et al. (1994, P94), as well as a mixture with “astronomical silicates” and graphite following the Draine & Lee (1984, DL84) prescription. One of the main differences between these mixtures is that DL84 consider that the carbon is in graphite while P94 assume that this element is in organics. Furthermore, P94 include other compounds, as water and troilite. We consider grains to be compact segregated spheres and calculate their efficiency factor Q_{abs} using a Mie scattering code (Wiscombe 1979, see more details in D’Alessio, Calvet & Hartmann 2001, hereafter DCH01). Optical properties for the compounds are taken from Warren (1984), Begemann et al. (1994) and P94.

4.2. Circumstellar disks

We assume that the two circumstellar disks observed at 7 mm by Rodríguez et al. (1998) are α accretion disks irradiated by the infalling envelope. The structure and emission of these disks is calculated as described in D’Alessio (1996) and DCH97. In short, the set of vertical structure equations are solved for a disk with a mass accretion rate \dot{M} around a star with mass M_* and radius R_* . The heating of the disks is determined by viscous dissipation and envelope irradiation. The viscosity ν is calculated with the α prescription (Shakura & Sunyaev 1973). Since data exist for each disk, we calculate the structure of each separately.

The disks are displaced relative to the center of symmetry of the system, thus, the envelope irradiation on each disk is not symmetric around its own rotational axis. However, since

the disks are small compared to the size of the envelope, we approximate the backwarming to be constant over each disk. The flux crossing the equatorial plane at a given distance from the envelope center is calculated solving the 2D radiative transfer throughout the envelope, as described in DCH97. The flux intercepted by each disk is then averaged over the disk annuli to give the irradiation flux on the disk, F_{irr} , or equivalently, the irradiation temperature, $T_{irr} = (F_{irr}/\sigma_R)^{1/4}$, which is used as input for the disk vertical structure calculations. The envelope model used in these calculations is the one that gives the best fit of the SED and to the large-scale brightness sub-mm distribution.

Since from present observations we cannot know if one of the disks is the dominant luminosity source in the system, we assume the same mass accretion rate and stellar parameters for both disks. We also assume that the disks have the same dust composition than the envelope. However, to explore the possibility of grain growth, we consider a_{max} to be a free parameter for each disk. Other input parameters are the inclination angle of each disk (between their rotation axis and the line of sight), the viscosity parameter α (or equivalently, its mass, DCH01), and the disk radius R_d .

4.3. Circumbinary Structure

In order to investigate whether the flattened structure at scales of 100-400 AU resolved at millimeter and submillimeter wavelengths corresponds to a circumbinary disk, we also included the contribution of this component. According to DCH97, for distances larger than ~ 20 AU from its center, the temperature T and surface density Σ of a disk surrounded by an optically thick envelope in which the heating is dominated by envelope irradiation can be represented by power laws in radius as $T \sim T_0(R/100 \text{ AU})^{-0.5}$ and $\Sigma \sim \Sigma_0(R/100 \text{ AU})^{-1}$, where R is the cylindrical radius from the disk center. The temperature T_0 is fixed by the envelope irradiation at 100 AU, and we take Σ_0 , the surface density at 100 AU, as a free parameter. The circumbinary disk has a fixed outer radius given by the envelope centrifugal radius R_c and an inner radius which is expected to be several times larger than the maximum separation between the circumstellar disks (Artymowicz et al. 1991). We present models with a grain size distribution similar to that in the extended envelope and that in the circumstellar disks, as the two extreme possibilities for the state of the dust in this disk.

5. MODEL RESULTS

In this section, we discuss the combination of parameters characterizing each one of the components of the L1551 IRS 5 system that can reproduce self-consistently the observational constraints. We have arranged the section according to the interpretation of a main constraint, but it should be kept in mind that the results for all components are interdependent and the present ordering just aims to make their description easier.

5.1. Large scale fluxes

5.1.1. Envelope SED

Each range of wavelengths in the SED of the envelope is sensitive to different parameters. The observed peak flux and its corresponding wavelength, which occurs generally at the far infrared (IR) range, depend mostly on the density of the envelope, which fixes the scaling ρ_1 , with a weak dependence upon the total luminosity of the system (see trends of KCH93 for low mass protostars and Osorio et al. 1999, for high mass protostars). On the other hand, the mid and near-IR fluxes are sensitive to the η parameter, the inclination to the line of sight i , and the centrifugal radius R_c . The radius of the envelope is determined by the large scale spatial intensity profiles (§5.2) and we take it as ~ 8000 AU.

The apparent luminosity of the system (calculated by direct integration of the observed SED, that would correspond to the luminosity of an isotropic source) is $L_{app} = 25L_{\odot}$, and it is an indicator of the total luminosity L_{tot} . For a given total luminosity and model, the apparent luminosity depends on the inclination of the system to the line of sight, especially in systems with a high degree of flattening. For instance, for $\eta = 2.5$, the ratio L_{app}/L_{tot} goes from ~ 1.4 if the system is seen pole-on, $i = 0$, to ~ 0.5 , for edge-on systems. Fortunately, for the range of inclinations that produce the best fits to the observed SEDs, $L_{app}/L_{tot} \sim 1$. Given the approximations in our treatment, specially the assumption of spherical symmetry for the envelope temperature distribution, we take here that $L_{tot} = L_{app}$.

The observed flux at the peak of the SED indicates a value of $\rho_1 \sim 4.5 \times 10^{-13} \text{ g cm}^{-3}$, which also consistently results in high fluxes for the large beam size observations in the submillimeter and millimeter ranges (§5.2). This value of ρ_1 , is the maximum density that can produce the high millimeter fluxes without too much extinction in the mid-infrared. The luminosity and ρ_1 are similar to those found by KCH93 for L1551, who considered envelopes slightly flattened in their inner part by rotation as described by Terebey, Shu & Cassen (1984, hereafter TSC envelopes); however those models predict a very deep silicate feature

which is not observed.

The recent silicate ($10\mu\text{m}$) and water ice ($3\mu\text{m}$, $6\mu\text{m}$) features observed by ISO and SpeX place stringent limits on the envelope parameters and its geometry. Even in the case of moderate inclination angles, TSC envelopes predict too much extinction at short wavelengths and therefore features deeper than the observed ones. Flattened η envelopes with the same ρ_1 as in TSC envelopes, have less polar material and more equatorial material. So, at inclination angles to the line of sight closer to the rotation axis, these envelopes have less extinction than TSC envelopes.

To show the dependence of the SED on η , i , and R_c , we present model SEDs for different values of these parameters, with L and ρ_1 fixed by the considerations above, and compare them with observations (§2). Further constraints come from other evidences. The nearly pole-on case ($i = 10^\circ$) is ruled out because the outflow extends considerably in the plane of the sky, with well-separated red- and blueshifted CO outflow lobes (Snell et al. 1980). In addition, it is likely that the binary system formed out of lower angular momentum material than is currently falling in; moreover, the evidence for a circumbinary disk also suggests that infalling material has a larger specific angular momentum than that of the binary separation. For these reasons, we will consider centrifugal radii larger than the maximum separation of the binary sources (~ 40 AU). Figure 3 (solid line) shows the model SEDs for $R_c = 300$ AU for different inclinations and values of η . Model SEDs in Figure 3 were calculated with abundances of silicates and graphite consistent with DL84 and an abundance for water ice lower than P94 by a factor of two. We will consider the effects of dust opacities in more detail in §5.1.2.

In general, all models for high inclination angles ($\sim 80^\circ$) predict too little near and mid-infrared emission, regardless of the degree of flattening (η parameter). As discussed above, models with roughly spherical envelopes ($\eta = 1.5$, similar to the case of TSC envelopes) have too much extinction along of the line of sight and therefore exhibit deeper absorption features than models which assume flatter envelopes. Thus, models for flattened envelopes and with moderate inclinations explain better the observed SED; in particular the best fits are obtained at inclination angles $i \sim 50^\circ$ and $\eta \sim 2.5$ for the case of $R_c = 300$ AU, which we adopt as our fiducial model. The angle-averaged density and temperature distributions of this model are shown in Figure 4.

The upper panel of Figure 5 compares observations with model SEDs calculated for $i \sim 50^\circ$, $\eta \sim 2.5$ and $R_c = 50, 300$, and 500 AU. All these models, with the same ρ_1 , result in similar millimeter and centimeter fluxes because at these wavelengths the envelope is optically thin and the emission comes from large scales. However, the near and mid-IR fluxes are much more sensitive to η , i , and R_c . The model with small centrifugal radius has

too much extinction along of the light of sight resulting in too deep silicate and ice features; the model with large R_c produces too little absorption. The parameters η , R_c , and i are somewhat interchangeable (HCB96); for instance, both an increase in η or in R_c result in low mean densities in the inner envelope. However, there are differences. As R_c increases, material tends to pile up at larger distances from the luminosity source on the equatorial plane; conversely, if R_c is small, even if the envelope is very flat there is material near the source and thus heated to higher temperatures. So, model envelopes with large η and small R_c tend to have higher near and mid-IR fluxes than low η models with large R_c , as shown in the lower panel of Figure 5. The parameters are thus fairly well constrained when aiming to fit a large range of wavelengths.

5.1.2. Effect of dust opacities on the envelope SED

One of the main uncertainties in determining the emission of YSOs lies in the dust opacity, since the dust properties are not well known. Several models for the dust opacities have been used so far in the interpretation of the SED of L1551 IRS 5, from interstellar medium dust (KCH93) to mixtures of segregates and aggregates grains, the latter with cores of silicates covered by ice mantles (White et al. 2000). They all are adjusted to fit the observations, so it is still not clear which is the best representation of the grains for this object.

In this work, we compare two mixtures that have been widely quoted in the literature of YSO in recent years and determine which gives the best fit to the observations. We calculate models for the mixture proposed by P94 for molecular envelopes, which includes olivine, organics, troilite, and water ice, with mass fractional abundances with respect to gas of $\zeta_{sil} = 0.0034$, $\zeta_{org} = 0.0041$, $\zeta_{tro} = 0.000768$, $\zeta_{ice} = 0.0012$. We also use the DL84 mixture, which characterizes the interstellar medium; this mixture consists of grains of graphite and “astronomical” silicates with a mass fractional abundances of $\zeta_{sil} = 0.004$ and $\zeta_{gra} = 0.0025$. We have added water ice to the DL84 mixture, to account for the observed water ice bands, with abundances similar or lower than that in the P94 mixture, as required to fit the observations. However, our mixtures do not consider the ice feature at $6 \mu\text{m}$ for the lack of optical constants in this band. Furthermore, in the case of DL84 mixture we increase slightly the silicate abundance ($\sim 20 \%$) to improve the fit at the near IR.

The upper panel of Figure 6 shows the model SED calculated for the parameters of the fiducial model with three different dust mixtures: P94, P94 but with ice with approximately half of the abundance in P94, which we call P94M, and DL84, again with ice with approximately half of the abundance in P94, which we call DL84M. As discussed in §5.1.1,

the model SED with DL84M at $i \sim 50^\circ$, gives the best fit to the near to far infrared SED. The water ice abundance is so high using P94 that the feature at $3 \mu\text{m}$ is very strong, much more than in the observations and a feature of water ice at $12 \mu\text{m}$ appears which is also inconsistent with the observations. However, even with a reduced water ice abundance, the P94M SED is different from the DL84M SED: the near-IR are higher, while the mid IR flux is lower which is in conflict with the observations.

The lower panel of Figure 6 compares the P94M and the DL84M opacities. One important difference between the two mixtures occurs in the near infrared range ($\sim 1\mu\text{m} - 5\mu\text{m}$), where the total opacity is mainly due to the carbon component of the mixture and this element can be either in graphite or organics. Although the abundance of organics (P94M) is higher than that of graphite (DL84M), its extinction in this interval is lower than that of graphite (see the behavior of the curves of these components in Fig. 6). Since the opacity is lower in the P94M mixture, the inner hot regions are more exposed with this mixture and the emergent flux is higher around $2\mu\text{m}$. However, also because the opacity is lower in the near-IR range, where most of the light from the circumstellar disks heating the envelope arises, the P94M inner envelope has a temperature ~ 0.8 times cooler than the DL84M envelope. In the mid-IR, the opacities for both mixtures have more similar values, so the depths where $\tau_\lambda \sim 1$ are approximately the same. Since the same spatial regions are contributing to the emission, but they are cooler for P94M, the emergent flux is lower. Because of these differences, we could not find any combination of parameters (i, R_c, η) that fitted the SED using the P94 mixture, even with lower ice content.

5.2. Millimeter Spatial Intensity Profiles

In this section, we consider the density distribution at large scales, inferred from the millimeter spatial intensity profiles in the SCUBA images of Chandler & Richer (2000, CR00). A comparison in two dimensions between the SCUBA images of CR00 and our predicted images is not possible because the JCMT beam is asymmetric and time variable along the observing run (see CR00 for details). Therefore, we averaged both the model and the data in circular annuli centered at the peak position. This yields a mean spatial intensity profile, $I(p)$ where p is the angular radius from source center. We simulate the observation at each wavelength convolving the output model with the approximate beam given by CR00; the model includes the envelope, the circumstellar disks, and the circumbinary disk. These components are calculated with the parameters that give the best fit to other observables, as determined in §5.1.1, 5.3, and 5.4.

Figure 7 compares the observed and the predicted spatial profiles at 450 and $850 \mu\text{m}$,

with observational errors from CR00. Following CR00, we subtracted the intensity at $60''$ from both the observations and the model. The dotted line shows the predicted emission without the circumbinary disk; the solid line includes all components of the system, showing the importance of the circumbinary disk at small and intermediate scales. The combined model provides a good fit to the observations, specially for $850\mu\text{m}$, which has the highest signal-to-noise (CR00).

To indicate the effects of flattening in the envelope, we show in Figure 7 model intensity profiles calculated along the minor (rotational) axis and the major (equatorial) axis of the envelope. The fact that the observed profile is closer to that of the lower intensity minor axis suggests that there is less material at large scales than expected, even for a flat envelope, which may be due to the effect of the wind/jet.

5.3. Circumstellar disk SEDs, 7 mm images and near IR CO absorption

The millimeter observations at high angular resolution can be used to fit the properties of the circumstellar disks, since the contribution of the envelope and circumbinary disk are resolved out (Rodríguez et al. 1998 and references therein; Looney et al. 1997; also see Table 1), and long-wavelength data indicate that contamination by free-free emission from ionized outflows is unlikely (Rodríguez et al. 1998.)

Since we are assuming that the system luminosity arises in the disks, we can equate $L_{tot}/2$ to the accretion luminosity of each disk, $L_{acc} = GM_*\dot{M}/R_*$. Another constraint comes from the maximum effective temperature in the disk for a steady viscous disk model, $T_{max} = 0.29 (GM_*\dot{M}/R_*^3\sigma)^{1/4}$, which we can equate to ~ 5000 K, from estimates of the optical scattered light spectrum (Stoeckle et al. 1988). Combining these two constraints, we obtain $R_* = 1.4R_\odot$ and $(M_*/0.3M_\odot)(\dot{M}/2 \times 10^{-6}M_\odot \text{ yr}^{-1}) \sim 1$. We adopt $M_* \sim 0.3M_\odot$, close to the value expected for a typical low-mass T Tauri star near the birthline (Stahler 1988; Hartmann, Cassen, & Kenyon 1997), so $\dot{M} \sim 2 \times 10^{-6}M_\odot \text{ yr}^{-1}$. (Note that for an α disk, the surface density $\Sigma \propto \dot{M}/\nu \propto \dot{M}M_*^{1/2}$, so we need to specify \dot{M} and M_* separately).

Figure 8 shows the dependence of observables on the disk model parameters. On the left panel, we show the flux at 7 mm vs I_{max} , which is the maximum intensity of the disk model image at this wavelength, calculated by convolving the emergent intensity with a $0''.062 \times 0''.052$ gaussian beam. The observed values of these quantities and the beam size are taken from Rodríguez et al. (1998). Results are shown for different inclination angles (measured by $\mu = \cos i$), viscosity parameter α (or \sim disk mass), and disk radius R_d , with values indicated in the figure caption. In the right panel of Figure 8, we show the total

flux at 2.7 mm vs the slope between 2.7 mm and 7 mm, defined as $n = -[\log(F_{7\text{mm}}) - \log(F_{2.7\text{mm}})]/[\log(7) - \log(2.7)]$ for different inclination angles and grain maximum sizes.

The mm flux increases with disk radius R_d , as expected, but the maximum intensity is almost constant with R_d because I_{max} arises in the inner ~ 7 AU, for a $\sim 0''.05$ beam. The flux also increases when the inclination angle decreases (μ increases), because these disks are optically thick in the mm wavelength range; these are bright compact disks, with smaller sizes and larger mass accretion rates than the typical Classical T Tauri disks, usually optically thin at radio frequencies.

The dependence of the emergent mm flux on the other parameters of the model also reflects optical depth effects. The upper panels of Figure 9 show the disk total vertical optical depth, τ_ν , at 2.7 mm and 7 mm for a_{max} equal to 200 μm (left column) and 600 μm (right column). At both wavelengths, the optical depth is greater than one. The lower panels of Figure 9 show relevant temperatures for the disk; in particular, T_c is the temperature at the midplane, T_{phot} is the photospheric temperature, and T_{vis} is the effective temperature corresponding to viscous heating alone (DCH97). In a very rough approximation, $T_{phot}^4 \sim T_{vis}^4 + T_{irr}^4$, where T_{irr} is determined by envelope irradiation. At small radii, $T_{phot} \sim T_{vis}$, but as radius increases, T_{phot} approaches $T_{irr} \sim 120$ K, the irradiation temperature provided by the fiducial envelope model (§5.1.1). On the other hand, the Rosseland mean optical depth for $R \lesssim 13$ AU in these disks is so high that the midplane temperature is not very sensitive to envelope irradiation; it is mostly determined by local viscous energy trapped close to the midplane (D'Alessio et al. 1999), as $T_c \propto T_{vis}\tau_R^{1/4}$, where τ_R is the vertical Rosseland mean optical depth, in the diffusion approximation.

The temperatures at which the optical depths at 2.7 mm and at 7 mm become ~ 1 are also indicated in Figure 9. These temperatures would be approximately the brightness temperatures at those wavelengths if the disks were pole-on, so they reflect the characteristic emergent intensity. As already pointed out by Rodríguez et al. (1998), at mm-wavelengths the disk radiation emerges from a depth close to the midplane. As a consequence of this, the disk emission is characterized by a temperature close to T_c which is much higher than the disk photospheric temperature because these are very optically thick disks. This explains why the disks have a brightness temperature higher than expected for the photosphere of a viscous disk, even with a high mass accretion rate $\sim 2 \times 10^{-6} M_\odot \text{ yr}^{-1}$ and illustrates the importance of constructing detailed physical vertical structure models reflecting the actual temperature gradients, and also the power of interferometric imaging in the mm range to probe the disk interior.

Figure 8 shows that the mm fluxes decrease with increasing α . The reason for this is that the surface density of an α viscous disk can be written as $\Sigma \propto \dot{M}/\alpha T_c$, so in the diffusion

approximation, $\Sigma \propto \alpha^{-4/5}$ and $T_c \propto \alpha^{-1/5}$. As α decreases, the midplane temperature and thus the flux increase, although slightly; the flux only increases by a factor of ~ 1.3 as α decreases by a factor of ~ 6 . Given the low dependence of T_c on α , the mass of the disk varies approximately as α^{-1} ; we have indicated in the figure the disk mass that corresponds to each of the models shown.

The mm fluxes and slope depend on the dust opacity, and in particular, on the maximum grain size a_{max} , although the disks are optically thick. This is a consequence of the fact that as the dust opacity changes, it affects both the height in the disk where $\tau_\nu \sim 1$, and the vertical thermal distribution (in the regions of the disk where the opacity is dominated by dust.) The larger the a_{max} , the smaller the τ_R , which is similar to the optical depth in the mid-IR for the range of temperatures in the disk (cf. DCH01); thus, as a_{max} increases, the midplane temperature decreases. In contrast, the mm opacity increases with a_{max} (cf. DCH01). However, the increase is larger for wavelengths around 2.7 mm for the range of sizes shown in Figure 8. This is because spherical grains, with a real refraction index $n > 1$, show an opacity enhancement around $\lambda \sim 2\pi < a >$, for an average grain radius $< a >$ (cf. Miyake & Nakagawa 1993; P94; DCH01). This effect produces a larger contrast in opacity between 2.7 and 7 mm when a_{max} increases, in the range of sizes considered, which then implies a larger contrast between the temperatures $T(\tau_\nu \sim 1)$ at both wavelengths as a_{max} increases. The difference in $T(\tau_\nu \sim 1)$ explains why the slope of the mm SED decreases as a_{max} increases. The consideration of other kind of grain shapes or porosity will tend to reduce or eliminate this enhancement of opacity (e.g., Miyake & Nakagawa 1993) making the effect of a_{max} on the slope of the mm SED less noticeable.

Figure 8 shows boxes centered in the observations of the northern disk with sides given by the observational uncertainties. A similar analysis can be made for the southern disk. The resulting model parameters adopted for each disk are shown in Table 2, with uncertainties given by the ranges analyzed in Figure 8.

The SED of an individual circumstellar disk for inclinations $i = 0^\circ$ and $i = 60^\circ$ is shown in the left panel of Figure 10, as well as the interferometric data for the northern disk from Looney et al. (1997) and Rodríguez et al. (1998). The ISO data is shown as a reference. The SED has been attenuated by the optical depth of the envelope model that produces the best fit to the IR SED (§5.1). At low inclinations, disk emission results in too much near-IR. However, at inclinations that produce the best fit to the mm data (cf. Figure 8), the near-IR emission of the disks drops because the disks are so flared that the outer regions of the disks attenuate the inner disk emission along the line of sight. To illustrate this, we show in the right panel of Figure 10 the cosine of the critical inclination angle $\mu_c(R)$, such that the inner disk is attenuated for values of inclinations $\mu < \mu_c(R)$, for a disk of radius

R . The critical angle is defined as $i_c = \cos^{-1} \mu_c$, such that $\mu_c = z_c / (z_c^2 + R^2)^{1/2}$, and the height z_c is that where the optical depth along a ray from the star to a point in the disk at radius R is unity. The optical depth is evaluated at a wavelength where radiation from the inner disk, with $T \sim 4500$ K, is expected to peak. Two disk models are shown in the right panel of Figure 10, a purely viscous disk and a viscous disk irradiated by the envelope, with parameters that provide the best fit to the mm data. The self-occluding effect is much more important in the case of the irradiated disk because the atmosphere at large radii is much hotter and has a larger scale height than the pure-viscous case; specifically, the atmosphere of the outer disk occults the inner disk when its axis is inclined by $\mu < 0.4$ ($i > 66^\circ$) to the line of sight for the non-irradiated disk and by $\mu < 0.6$ ($i > 50^\circ$) for the irradiated disk (for $R_d \sim 10$ AU). For the case $i = 60^\circ$ shown in Figure 10, the optical depth due to the disk along a ray that passes through the center of the star is $\tau(1 \mu m) \sim 25$. This self-occultation of the disk, arising as a consequence of other observational constraints, explains nicely the fact that at the near infrared, the observed emission is extended (Lucas & Roche 1996). In our interpretation, the near-IR emission is mostly light from the inner disk scattered out by the outer disk and the surrounding envelope towards the observer, and thus it is seen as an extended rather than a pointlike source.

We have calculated the flux of the first overtone CO bands in the near infrared, formed in a disk atmosphere whose density and temperature profiles are determined using the same mass accretion rate and stellar parameters as each of the binary disks, following the procedures in Calvet et al. (1991). Figure 11 shows the result of these calculations for an inclination angle $\sim 60^\circ$, convolved with a resolution of $R=2000$. At this resolution, disk spectra for inclinations less than $\sim 70^\circ$ would be similar. Disk models with parameters that reproduce the long wavelength, the near-infrared and total emission constraints predict very well the observed strengths of the first two CO first overtone bands in our SpeX spectrum, as shown in Figure 11, providing an additional confirmation of the disk structural parameters.

Since the inner disks are occulted, the flux at $2.3 \mu m$ is actually radiation from the inner disks scattered by dust at the edges of the disks and in the envelope (a similar conclusion was reached by White et al. 2000). A contribution from thermal emission of the hot dust in the innermost regions of the envelope should be added to the light scattered from the disk, which would tend to decrease the strength of the absorption; as more material is located in these hot regions, the stronger the veiling expected in the CO bands, as discussed in Calvet, Hartmann, & Strom (1997). As shown in that paper, the veiling roughly scales with the density at the dust destruction radius. With a mean density of $\sim 4 \times 10^7 \text{ cm}^{-3}$ from our envelope calculations, we obtain a veiling ~ 0.3 scaling from their results. This is likely to be an upper limit, since we expect more evacuation in the η models than in the TSC models used in Calvet, Hartmann, & Strom (1997), which is consistent with the low veiling of the

CO bands indicated in Figure 11.

5.4. Circumbinary Disk SED

As discussed in §2 and §4.3, the observations of Keene & Masson (1990), Lay et al. (1994), Hogerheijde et al. (1997) suggest dust emission with a scale of 100-400 AU. Looney, Mundy & Welch (1997) also found evidence of a structure of similar size from emission at 2.7 mm and they estimated that this structure could be a circumbinary disk with a mass of $\sim 0.04M_{\odot}$. Following these suggestions, we have included a circumbinary disk in our model. The outer radius of this disk is limited by the centrifugal radius, as discussed in §4.3; from the result of our envelope SED modeling, §5.1.1, we infer $R_c \sim 300$ AU, approximately in agreement with expected sizes. We have taken the inner disk radius as 120 AU, three times the apparent separation between the circumstellar disks.

Figure 12 shows the fluxes for this structure. Fluxes at $450\mu\text{m}$ and $850\mu\text{m}$ are the fluxes added to the envelope to fit large-scale intensity distribution profiles, §5.2. The latter flux agrees with the flux obtained by Lay et al. (1994). Fluxes at 2.7 mm have been estimated by Keene & Masson (1990), Looney et al. (1997) and Hogerheijde et al. (1997) and the flux at 3.4 mm has been estimated by Hogerheijde et al. (1997). For these fluxes we have subtracted the contribution from the circumstellar disks (§5.3) since at 2.7 and 3.4 mm their emission is substantial.

The irradiation flux produced by the fiducial model of §5.1.1, yields a temperature at 100 AU of $T_0 \sim 55\text{K}$. With this temperature, we model the fluxes in Figure 12 to obtain the density distribution scaling Σ_0 ; this value is very sensitive to the adopted opacity. Figure 12 shows fits for a dust size distribution similar to that in the envelope ($a_{max} = 0.3\mu\text{m}$) and a dust size distribution as in the circumstellar disks ($a_{max} = 400\mu\text{m}$). The mass surface density at 100 AU for these models is $\Sigma_0 = 34\text{ g cm}^{-2}$ and $\Sigma_0 = 1.3\text{ g cm}^{-2}$, respectively, with corresponding masses of 0.4 and $0.02 M_{\odot}$. The large difference in disk mass is due to the drop of mm opacity as a_{max} decreases. The mass obtained by Looney et al. (1997) is near our lower limit, because they use an opacity consistent with large grains. Our models for the circumbinary disk are little restricted, however we favor the model obtained with the envelope dust, since material from the envelope is arriving on the equatorial plane of the system mostly near R_c , raining on top of the circumbinary disk. Interferometric observations of high rotational molecular line transitions (such as those that will be achievable with the SMA in the near future), that would trace the warm component of the gas, together with a more detailed modelling of these line emission could strengthen the case for the existence of the circumbinary ring and determine better its physical parameters.

5.5. Summary of results

To summarize, the far-IR SED fluxes the density in the envelope, while the degree of flattening, the centrifugal radius and the inclination are mostly determined by the near and mid-IR fluxes. The submillimeter images also constrain the density of the envelope, at scales of hundreds of AU, they require an additional contribution from the circumbinary disk. The millimeter interferometric images and fluxes, as well as the total luminosity of the system, the optical and near-IR spectra, and the near-IR images determine the properties of the circumstellar disks. The circumstellar disks are the source of the luminosity that heats the envelope; in turn, envelope irradiation is a key element in the heating of the disks in the system. Figure 13 shows the overall fit to the data, indicating each component separately. The parameters characterizing each component are given in Table 2.

6. DISCUSSION

One of the challenges to models posed by recent observations is the detection of giant envelopes (as determined from observations by Chandler & Richer 2000 for L1551 IRS 5, and by Shirley et al. 2000, Motte & André 2001, Larsson, Liseau & Men'shchikov 2002 in other protostars) combined with a limited depth in the silicate absorption feature (White et al. 2000). As discussed in §5, previous envelope models predict silicate features that are too deep (Butner et al. 1991; KCH93) even with small envelopes; increasing the envelope limits makes the problem worse. The flattened density distribution of the sheet collapse or η model alleviates this problem by reducing the amount of extinction along the line of sight to the central region. As observations suggest that the envelope of IRS 5 is indeed flattened, this solution to the silicate feature problem seems reasonable.

The value of ice abundance ($\text{H}_2\text{O}/\text{H} \lesssim 4 \times 10^{-5}$) require to fit the envelope SED, so that the absorption to 3 microns is reproduced and that at the same time the absorption of water ice at 12 microns does not appear, is a factor of two lower than determinations of P94 and Tielens et al. (1991). This latter author determined approximately the abundance in L1551 IRS 5 from the optical depth of water ice, silicates features and assuming standard dust-to-gas correlations. With our abundance we estimated a water ice column density of $\sim 1.5 \times 10^{19} \text{ cm}^{-2}$ at the radius where the sublimation temperature occurs ($\sim 100 \text{ K}$, for water ice cf. Sandford & Allamandola 1993) in our best fit to the envelope SED. However, a determination of the column density deduced from the optical depth at 3.08 microns from our spectrum using $I = I_o e^{-\tau}$ and $N_{dust}(\text{H}_2\text{O}) = \tau_{3.08} \Delta\nu_{1/2} / A$ (Lacy et al. 1984; Sandford et al. 1988), where A is the band strength and $\Delta\nu$ is the full-width at half maximum intensity, provides a lower value ($\sim 3.8 \times 10^{18} \text{ cm}^{-2}$, consistent with that found by Tegler et al.

(1993), and within a factor of two of that determined by White et al. 2000, using the same method). The discrepancy with our value inferred from the best fit might be caused by determinations of the optical depth from $I = I_o e^{-\tau}$, where I_o and I are the intensities measured from the spectrum at continuum level and at the position of the ice absorption respectively, can underestimate the optical depth and then the column density by ignoring local emission in the radiative transfer. Thus, one must to take the value of the column density inferred in this way only as a lower limit.

We also found that the P94 mixture with no graphite but organic grains was not able to fit simultaneously the near-infrared and millimeter range of the spectrum. While we find reasonable fits to the SED with the modified Draine & Lee opacities, we do not therefore conclude that graphite must necessarily be present, merely that the overall opacity curve must resemble the results for this mixture. Other models, for example those of Li & Greenberg (1977) with organic refractory mantles for silicate core grains, might also work well.

We require slightly different inclination angles for the accreting disks at the center of the IRS 5 system in comparison with the inclination adopted for the envelope. However, the difference is small, considering the assumptions and simplifications involved in our calculations. It is also quite possible that the jets and therefore their originating disks are not perfectly aligned (Rodríguez et al. 1998). The circumstellar disks are quite massive (see Table 2) compared to typical Classical T Tauri disks. The disk models are gravitationally unstable against axisymmetric perturbations for $R > 6$ AU and $R > 8$ AU, for the northern and southern disks respectively, and the Toomre parameter at R_d is $Q_T(10AU) \sim 0.5$ and 0.8 , for each disk. Also the interaction between both disks and them with the circumbinary ring could strongly affect the disk structure and the pertinence of the α prescription can be questioned.

In our model, the envelope material falls mostly near the centrifugal radius, which is considerably outside the positions of the two disks. Using the value of ρ_1 for the envelope, the envelope infall rate is $\sim 7 \times 10^{-5} (M_{sys}/0.9M_\odot)^{0.5} M_\odot yr^{-1}$, where M_{sys} is the mass at the center, i.e., the sum of stellar and disk masses. Notice that the value of M_{sys} in our model is roughly consistent with the dynamical mass of the binary system recently estimated by Rodríguez et al. (2002). Thus, the mass infall rate of the envelope is an order of magnitude or more larger than the total accretion rate through the two disks, $\sim 4 \times 10^{-6} M_\odot yr^{-1}$. While these disk accretion rate estimates are somewhat model dependent, they are consistent with the total system luminosity; if the disk accretion rates were really as large as $7 \times 10^{-5} M_\odot yr^{-1}$, the total system luminosity for the protostellar mass-radius relation used above (roughly birthline values; Stahler 1988) would be roughly $L_{acc} = G\dot{M}M_*/R_* \sim 440L_\odot$, an order of magnitude larger than observed. This suggests that material may be

piling up, for example in the circumbinary ring or disk suggested by the interferometric observations at intermediate resolutions (§2, §5.4), and is not currently accreting in the disks. KCH93 noted a similar “luminosity” problem for Taurus Class I sources; in general, the infall rates estimated from the TSC models would produce accretion luminosities an order of magnitude higher than observed if the infalling material accreted at the same rate onto the central protostar. KCH93 also suggested that material is piling up onto outer disks without immediately and continuously accreting inward. In the case of IRS 5, we have for the first time additional confirmation of this suggestion, in that the disk accretion rate directly estimated from the mm observations is much lower than the infall rate.

It is unreasonable to suppose that material can pile up indefinitely in an outer circumbinary disk, at least when that disk accumulates a mass comparable to that in the central regions. Following the proposal of Kenyon & Hartmann (1991), KCH93 suggested that FU Orionis outbursts occur when disk material that has accumulated in outer radii becomes gravitationally unstable and catastrophically accretes in a burst. The FU Ori characteristics seen in the optical and near-infrared spectra features (Carr et al.1987; Stocke et al.1988) provide additional circumstantial evidence for this model. Circumbinary disk mass estimates are strongly dependent upon the assumed opacities, for a $M \sim 0.02 - 0.4M_{\odot}$ given from our fits, the disk may be gravitationally unstable supporting the fact that a FU Ori event is happening. The FU Ori outburst may be ending, with the circumbinary disk already having been emptied out; the current IRS 5 accretion rates are several times smaller than the typical FU Ori accretion rates at maximum, $\sim 10^{-4}M_{\odot}yr^{-1}$ (Hartmann & Kenyon 1996), consistent with a considerable decline from maximum accretion rate. In any event, our results emphasize the need to consider protostellar evolution with variable accretion rates, and the probable importance of differing disk accretion rates and envelope infall rates for studying evolution and fragmentation in protostellar disks.

7. SUMMARY AND CONCLUSIONS

Our main results can be summarized as follows:

1. The wealth of observational data available for L1551 IRS 5, in particular the observed SED by ISO and the water ice feature at 3 microns by SpeX has enabled us to develop detailed models for the circumstellar envelope, constraining its luminosity, geometry, infall accretion rate, and opacity.
2. We find that flattened collapse models with an inclination along the line of sight $\sim 50^{\circ}$, a total luminosity of $\sim 25 L_{\odot}$, mass $\sim 4 M_{\odot}$, infall accretion rate $\sim 7 \times 10^{-5} M_{\odot} yr^{-1}$

and a normal opacity laws, modified by changing the water ice abundance, enable us to fit simultaneously the ISO, SpeX observations and single dish submillimeter and millimeter fluxes that are mostly dominated by the emission of the large scale envelope.

3. We find that the a mixture as the proposed by Pollack et al. 1994 with no graphite but organic grains was not able to fit simultaneously the near-infrared and millimeter range of the spectrum. While we find reasonable fits to the envelope SED with the modified Draine & Lee opacities, we do not conclude that graphite must necessarily be present, merely that the overall opacity curve must resemble the results for this mixture.
4. At smaller scales than 2000 AU, the millimeter spatial intensity profiles in the SCUBA images suggest the presence of the circumbinary disk. We model this structure with a grain size distribution similar to that in the extended envelope and that in the circumstellar disks, as the two extreme possibilities for the state of the dust in this disk. We find that the mass of the circumbinary disk goes from 0.02 to 0.4 M_{\odot} for $a_{max} = 400 \mu\text{m}$ and $a_{max} = 0.3 \mu\text{m}$, respectively.
5. The properties of the circumstellar disks are inferred from high angular millimeter images and fluxes, optical spectra and near-IR image. We find that these disks are optically thick in the mm wavelength range; and are inclined an angle ($\sim 60^{\circ}$), so that their outer parts hide the emission from their inner parts. We also find that these disks have larger mass accretion rates ($\sim 2 \times 10^{-6} M_{\odot} \text{ yr}^{-1}$) than the typical Classical T Tauri disks, usually optically thin at radio frequencies.
6. The millimeter emission of the circumstellar disks emerges from a depth close to the midplane. As a consequence of this, the disk emission is characterized by a temperature much higher than the disk photospheric temperature. This explains why the disks have a brightness temperature higher than expected for the photosphere of a viscous disk, even with a high mass accretion rate and illustrates the importance of constructing detailed physical vertical structure models reflecting the actual temperature gradients, and also the power of interferometric imaging in the mm range to probe the disk interior.
7. The circumstellar disk models with parameters that reproduce the observational constraints, predict very well the observed strengths of the first two CO first overtone bands detected in our SpeX spectrum, providing an additional confirmation of the disk structural parameters.
8. In the case of L1551 IRS 5, we have for the first time the confirmation of the suggestion, that material is piling up onto outer disks without immediately and continuously

accreting inward since the disk accretion rate directly estimated from the mm observations is much lower than the infall rate, probably resulting in the accumulation of material in a circumbinary disk, possibly with occasional cascades of accretion into the binary system to produce FU Orionis eruptions.

Acknowledgments

We thank Claire Chandler for providing us the original SCUBA data of L1551 IRS 5 and Mario van den Ancker for help with the ISO data. Thanks as well to Robert Estalella and Maite Beltrán for providing a program to convolve our results with the observing beam of SCUBA camera. We also thank Guillem Anglada for useful discussions and helpful suggestions. J.M. would like to thank Bobby Bus and John Rayner for support at IRTF. M. O. acknowledges the fellowship from Conacyt, México and the NASA Origins of Solar Systems grant NAG5-9670. P. D. acknowledges the grant J27748E from Conacyt, México. We thank our referee for his/her thoughtful review of our manuscript and useful comments.

REFERENCES

- Adams, F.C., Lada, C.J., & Shu, F.H. 1987, *ApJ*, 312, 788
- Artymowicz, P., Clarke, C.J., Lubow, S.H., & Pringle, J.E. 1991, *ApJ*, 370, L35
- Begemann, B., Dorschner, J., Henning, T., Mutschke, H., & Thamm, E. 1994, *ApJ*, 423, L71
- Bieging, J.H. & Cohen, M. 1985, *ApJ*, 289, L5
- Butner, H.M., Evans, N.J. II, Lester, D.F., Levreault, R.M., & Strom, S.E., 1991, *ApJ*, 376, 636
- Calvet, N., Hartmann, L., Kenyon, S.J., & Whitney, B.A. 1994, *ApJ*, 434, 330
- Calvet, N., Patino, A., Magris, G.C., & D'Alessio, P. 1991, *ApJ*, 380, 617
- Calvet, N., Hartmann, L., & Strom, S.E. 1997, *ApJ*, 481, 912
- Carr, J.S., Harvey, P.M., & Lester, D.F. 1987, *ApJ*, 321, L71
- Cassen, P. & Moosman, A. 1981, *Icarus*, 48, 353
- Chandler, C.J., & Richer, J.S. 2000, *ApJ*, 530, 851 (CR00)
- D'Alessio, P. 1996, Ph.D. thesis, Universidad Nacional Autónoma de México, México
- D'Alessio, P., Calvet, N., & Hartmann, L. 1997, *ApJ*, 474, 397 (DCH97)
- D'Alessio, P., Calvet, N., Hartmann, L., Lizano, S., Cantó, J., 1999 *ApJ*, 527, 893
- D'Alessio, P., Calvet, N., & Hartmann, L., 2001 *ApJ*, 553, 321 (DCH01)
- Draine, B.T., & Lee, H.M. 1984, *ApJ*, 285, 89
- Dutrey, A., Guilloteau, S., & Simon, M. 1994, *A&A*, 286, 149
- Fridlund, C.V.M., Bergman, P., White, G.J., Pilbratt, G.L., & Tauber, J.A. 2002, *A&A*, 382, 573
- Fridlund, C.V.M., & Liseau, R. 1998, *ApJ*, 499, L75
- Hartmann, L., Boss, A., Calvet, N., & Whitney, B. 1994, *ApJ*, 430, L49
- Hartmann, L., Calvet, N., & Boss, A. 1996, *ApJ*, 464, 387 (HCB96)

- Hartmann, L., & Kenyon, S.J., 1996, ARA&A, 34, 207
- Hartmann, L., Cassen, P., & Kenyon, S.J. 1997, ApJ, 475, 770
- Hogerheijde, M.R., van Dishoeck, E.F., Blake, G.A. & van Langevelde, H. J., 1997, ApJ, 489, 293
- Keene, J., & Masson, C.R., 1990, ApJ, 355, 635
- Kenyon, S.J., Calvet, N. & Hartmann, L., 1993, ApJ, 414, 676 (KCH93)
- Kenyon, S.J., Dobrzycka, D., & Hartmann, L. 1994, AJ, 108, 1872
- Kenyon, S.J.& Hartmann, L.W. 1991, ApJ, 383, 664
- Lacy, J.H., Baas, F., Allamandola, L.J., van de Bult, C.E.P., Persson, S.E., McGregor, P.J., Lonsdale, C.J., & Geballe, T.R. 1984, ApJ, 276, 533
- Ladd, E.F., Fuller, G.A., Padman, R., Myers, P.C. & Adams, F.C., 1995, ApJ, 439, 771
- Larsson, B., Liseau, R., & Men'shchikov, A.B. 2002, A&A, 386, 1055
- Lay, O.P., Carlstrom, J.E., Hills, R.E., & Phillips, T.G., 1994, ApJ, 434, L75
- Li, A. & Greenberg, J.M. 1997, A&A, 323, 566
- Looney, L.W., Mundy, L.G., & Welch, W.J., 1997, ApJ, 484, L157
- Lucas, P.W. & Roche, P.F. 1996, MNRAS, 280, 1219
- Men'shchikov, A.B., & Henning, Th., 1997, A&A, 318, 879
- Miyake, K. & Nakagawa, Y. 1993, Icarus, 106, 20
- Momose, M., Ohashi, N., Kawabe, R., Nakano, T.& Hayashi, M., 1998, ApJ, 504, 314
- Moriarty-Schieven, G.H., Wannier, P.G., Keene, J., & Tamura, M. 1994, ApJ, 436, 800
- Motte, F., & André, P., 2001, A&A, 365, 440
- Mundt, R., Stocke, J., Strom, S.E., Strom, K.M., & Anderson, E.R. 1985, ApJ, 297, L41
- Osorio, M., Lizano, S., & D'Alessio, P., 1999, ApJ, 525, 808
- Pollack, J.B., Hollenbach, D., Beckwith, S., Simonelli, D.P., Roush, T. & Fong, W. 1994, ApJ, 421, 615 (P94)

- Rayner, J.T., Toomey, D.W., Onaka, P.M., Denault, A.J., Stahlberger, W.E., Watanabe, D.Y. and Wang, S.I. 1998, *Infrared Astronomical Instrumentation*, ed. A. M. Fowler, Proc. SPIE 3354, 468
- Rodríguez, L.F. et al., 1998, *Nature*, 395, 355
- Rodríguez, L.F., Curiel, S., Cantó, J., Loinard, L. & Torrelles, J.M., 2002, *Astrophysical Journal*, in press
- Saito, M., Kawabe, R., Kitamura, Y., & Sunada, K., 1996, *ApJ*, 473, 464
- Sandford, S.A. & Allamandola, L.J. 1993, *ApJ*, 417, 815
- Sandford, S.A., Allamandola, L.J., Tielens, A.G.G.M., & Valero, G.J. 1988, *ApJ*, 329, 498
- Shakura, N.I. & Sunyaev, R.A. 1973, *A&A*, 24, 337
- Shirley, Y.L., Evans, N.J. II, Rawlings, J.M.C., & Gregersen, E.M., 2000, *ApJS*, 131, 249
- Snell, R.L., Loren, R.B., & Plambeck, R.L. 1980 *ApJ*, 239, L17
- Stahler, S.W. 1988, *ApJ*, 332, 804
- Stocke, J.T., Hartigan, P.M., Strom, S.E., Strom, K.M., Anderson, E.R., Hartmann, L.W., & Kenyon, S.J. 1988, *ApJS*, 68, 229
- Strom, K.M., Strom, S.E., & Vrba, F.J. 1976, *AJ*, 81, 320
- Terebey, S., Shu, F.H., & Cassen, P. 1984, *ApJ*, 286, 529
- Tegler, S.C., Weintraub, D.A., Allamandola, L.J., Sandford, S.A., Rettig, T.W., & Campins, H. 1993, *ApJ*, 411, 260
- Tielens, A.G.G.M., Tokunaga, A.T., Geballe, T.R., & Baas, F. 1991, *ApJ*, 381, 181
- Walker, C.K., Adams, F.C., & Lada, C.J. 1990, *ApJ*, 349, 515
- Warren, S.G., 1984, *Applied Optics*, vol. 23, p. 1206
- White, G.J., Liseau, R., Men'shchikov, A.B., et al. 2000, *A&A*, 364, 741
- Wiscombe, W.J., 1979, *Mie scattering calculations: advances in technique and fast, vector-speed computer codes*, NCAR/TN-140 + STR, National Center for Atmospheric Research, Boulder, Colo.

Table 1. COMPILATION OF SUBMM AND MM OBSERVATIONAL DATA

λ (μm)	Instrument	Angular Resolution ($''$)	Flux Density (Jy)	Size (AU)	Refs.
350	JCMT	12	164	~ 8000	1
450	JCMT	11	94	~ 8000	1
730	JCMT	16	37	~ 4200	2
730	JCMT	16	3	~ 1300	2
750	JCMT	14	18	~ 8000	1
800	JCMT	17	8	\dots	3
850	JCMT	15	12	~ 8000	1
850	JCMT	16	17	~ 4200	2
870	JCMT-CSO	$\sim 1\text{--}4$	2.24	~ 80	4
1000	Hale Telescope	55	5.7	\dots	5
1100	JCMT	19	5	~ 5600	2
1100	JCMT	18	2.8	\dots	3
1300	IRAM	11	3	~ 10000	6
1300	12 m NRAO	~ 30	0.7	\dots	7
2700	OVRO	3	0.097	< 400	8
2700	BIMA ^a	0.3	0.045	< 25	9
2700	BIMA ^b	0.3	0.023	< 25	9
2730	OVRO	3	0.29	~ 2000	5
2730	OVRO	3	0.13	~ 50	5
3000	12 m NRAO	~ 60	0.7	\dots	7
3400	OVRO	6	0.081	< 400	8
7000	VLA ^a	0.05	0.0074	~ 10	10
7000	VLA ^b	0.05	0.0048	~ 10	10
13000	VLA ^a	~ 0.1	0.0020	\dots	10
13000	VLA ^b	~ 0.1	0.0015	\dots	10

^aNorthern disk.

^bSouthern disk.

References. — (1) Chandler & Richer 2000 (using SCUBA); (2) Ladd et al. 1995 (using the UKT14 bolometer); (3) Moriarty-Schieven et al. 1994 (using the UKT14 bolometer); (4) Lay et al. 1994; (5) Keene & Masson 1990; (6) Motte & André 2001; (7) Walker et al. 1990; (8) Hogerheijde et al. 1997; (9) Looney et al. 1997; (10) Rodríguez et al. 1998 and references therein.

Table 2. PARAMETERS OF THE MODEL

Envelope		
L_{tot} (L_{\odot})	25	
i (degrees)	50	
ρ_1 (g cm^{-3})	4×10^{-13}	
\dot{M}_{infall} ($M_{\odot} \text{ yr}^{-1}$)	7×10^{-5}	
R_c (AU)	300	
R_{out} (AU)	~ 8000	
η	2.5	
a_{max} (μm)	0.3	
Mass (M_{\odot})	4	
Circumbinary Disk		
i (degrees)	50	
Inner Radius (AU)	120	
Outer Radius (AU)	300	
a_{max} (μm)	0.3	
Σ_0 (g cm^{-2})	34	
Mass (M_{\odot})	0.4	
$Q_T(300 \text{ AU})$	0.01	
	Northern Disk	Southern Disk
M_* (M_{\odot})	0.3	0.3
R_* (R_{\odot})	1.4	1.4
i (degrees)	60	62
\dot{M}_{acc} ($M_{\odot} \text{ yr}^{-1}$)	2×10^{-6}	2×10^{-6}
R_d (AU)	13	12
a_{max} (μm)	200	400
α	0.0016	0.0047
M_d (M_{\odot})	0.25	0.1
$Q_T(10 \text{ AU})$	0.5	0.8

Note. — Assumed distance is 140 pc.

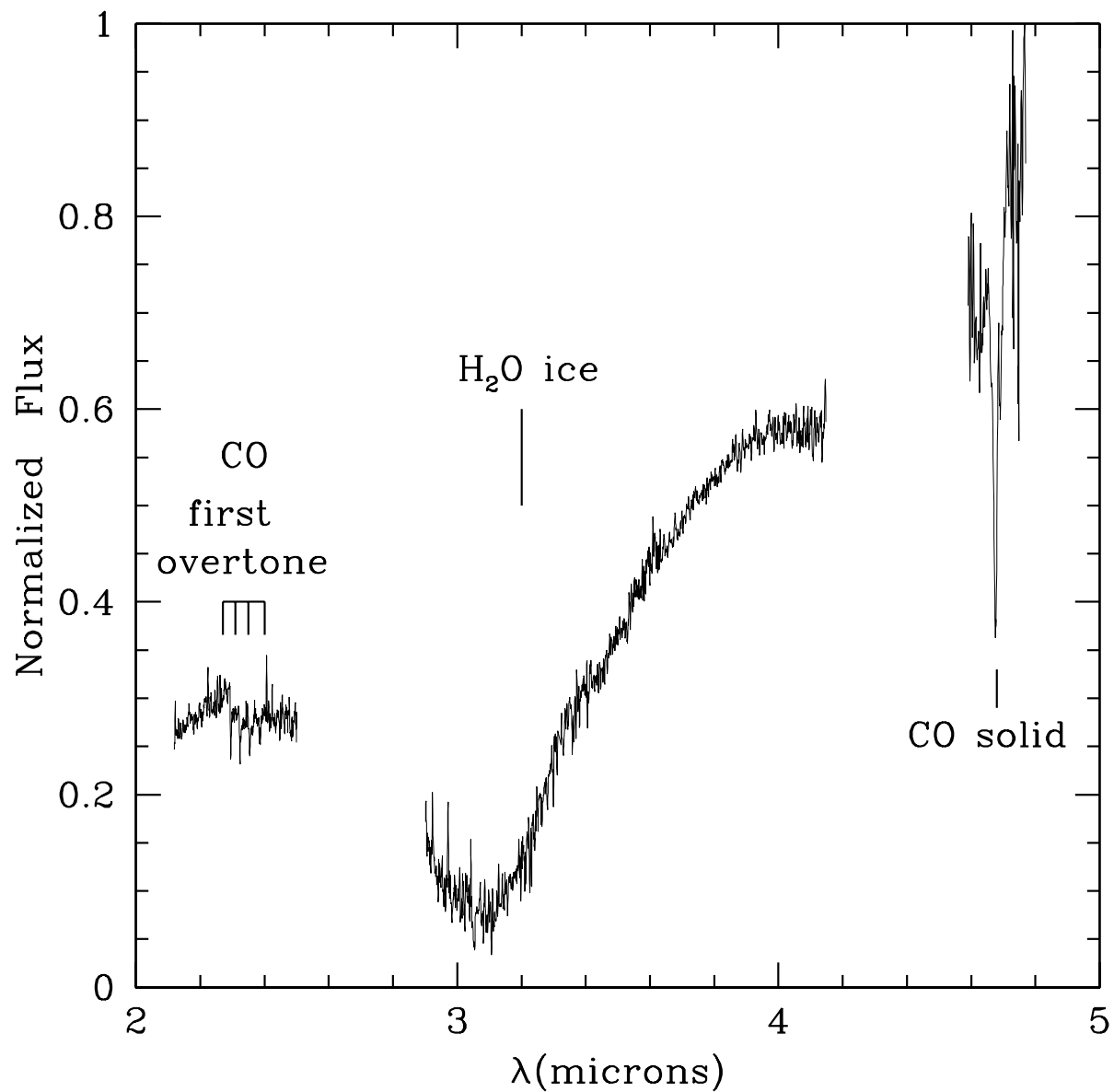


Fig. 1.— Near-infrared spectrum of L1551 IRS 5 obtained with SpeX. The telluric absorption lines have already removed. Spectral features mentioned in the text are marked.

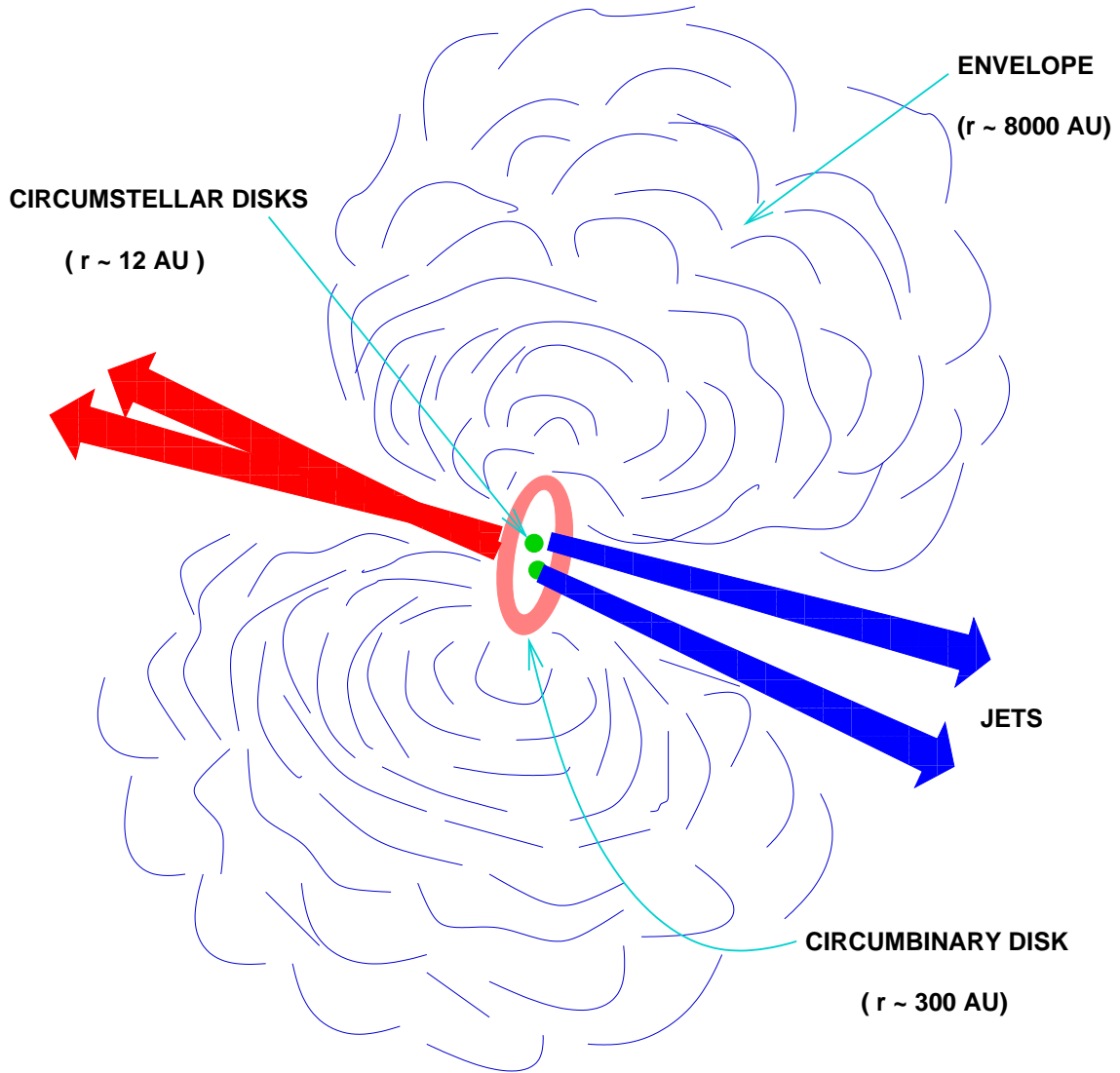


Fig. 2.— Sketch of the geometry of the model for L1551 IRS 5

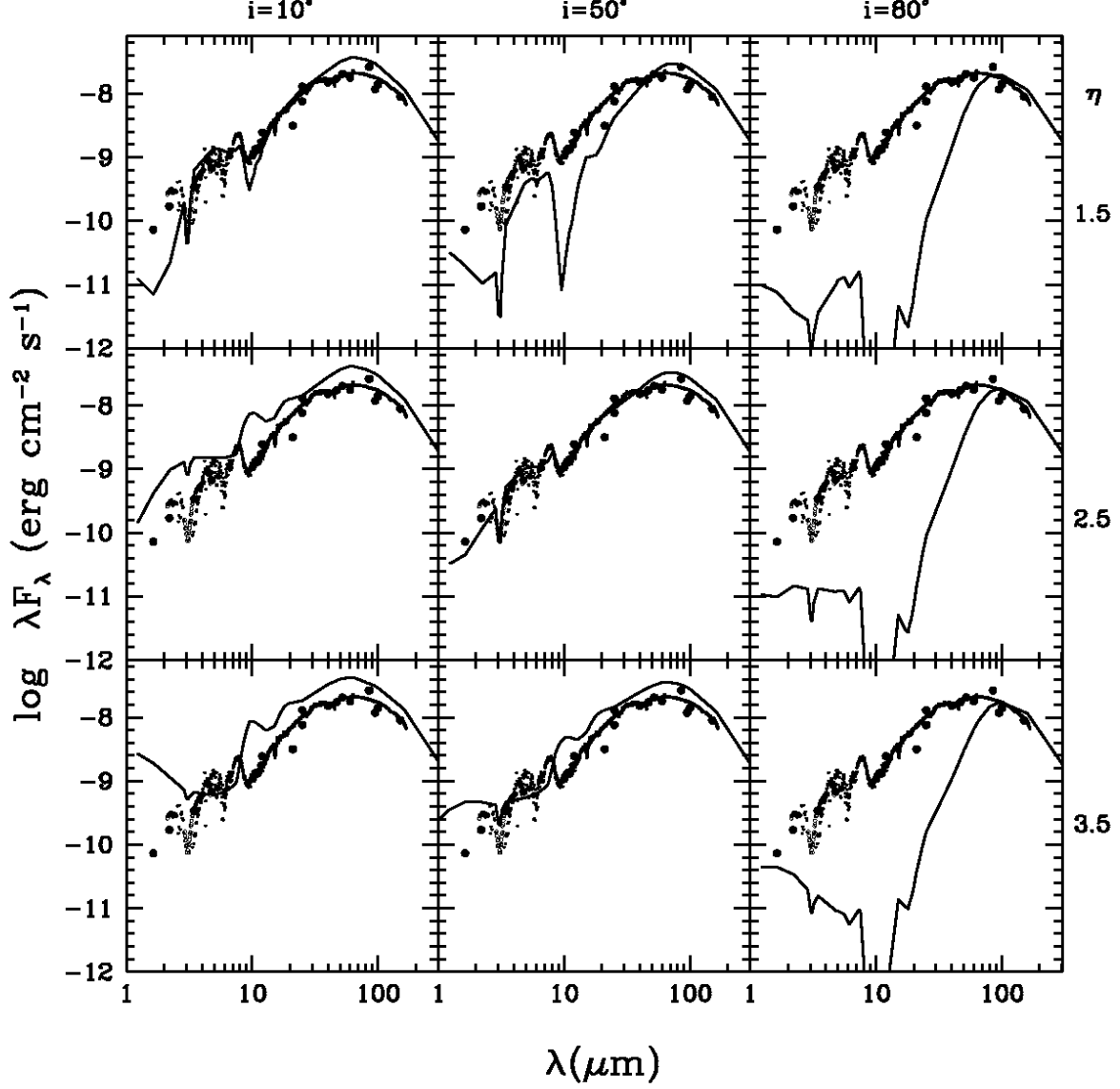


Fig. 3.— Grid of model SEDs for inclination angles $10^\circ, 50^\circ, 80^\circ$ (columns) and $\eta = 1.5, 2.5, 3.5$ (rows). All the models have $R_c = 300$ AU, $\rho_1 = 4.5 \times 10^{-13} \text{ g cm}^{-3}$, $L = 25L_\odot$, $D = 140$ pc, and an opacity with the Modified Draine & Lee mixture (see §5.1.2). ISO (filled-small dots), Spex (open-small dots) observations and photometry compiled by KCH93 (filled-big

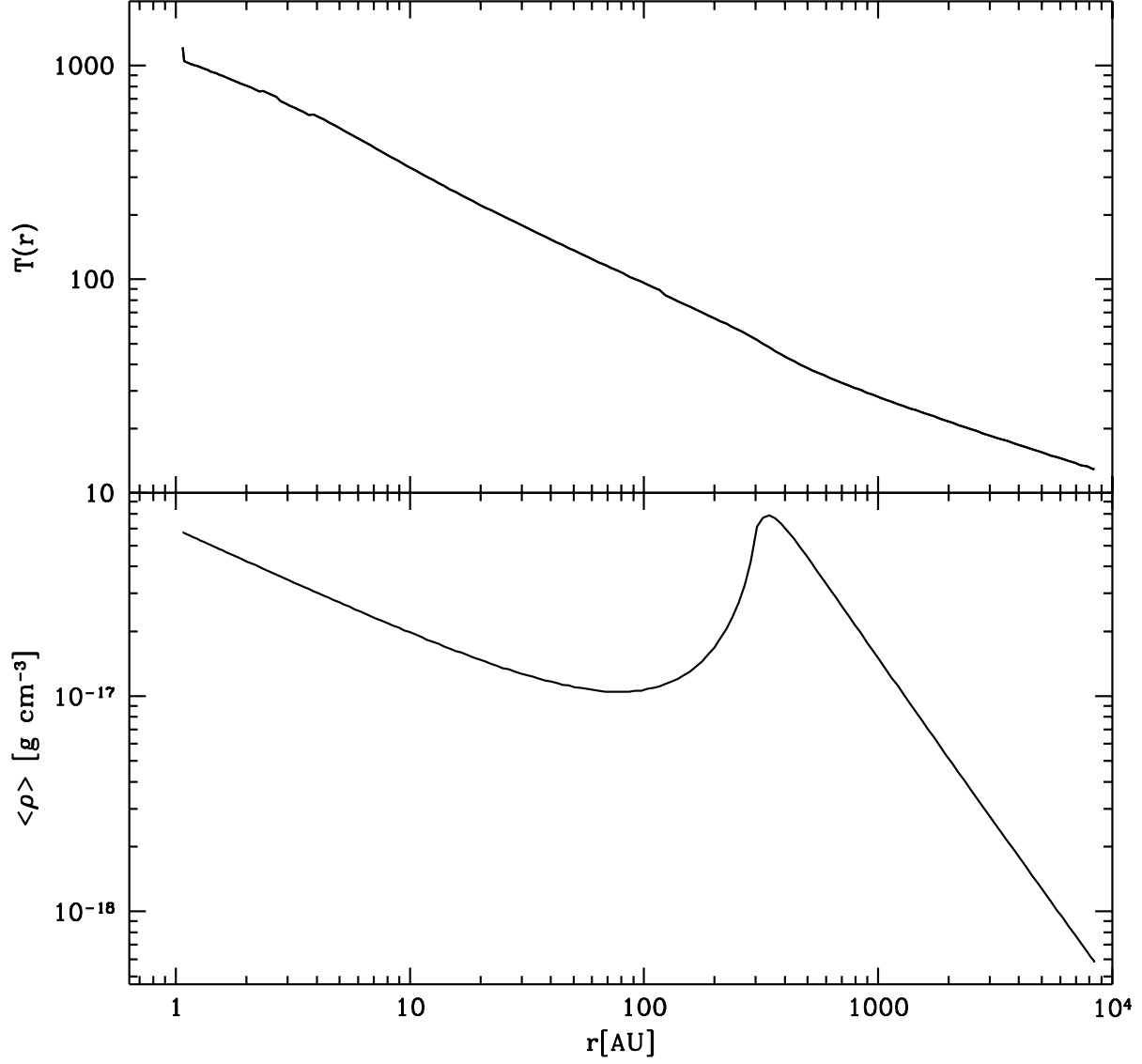


Fig. 4.— Temperature (upper panel) and angle-averaged density distribution (lower panel) of the envelope fiducial model: $i \sim 50^\circ$, $\eta \sim 2.5$ and $R_c=300$ AU (see §5.1.1). Inside the centrifugal radius the angular momentum of the infalling material causes departures from the radial free fall.

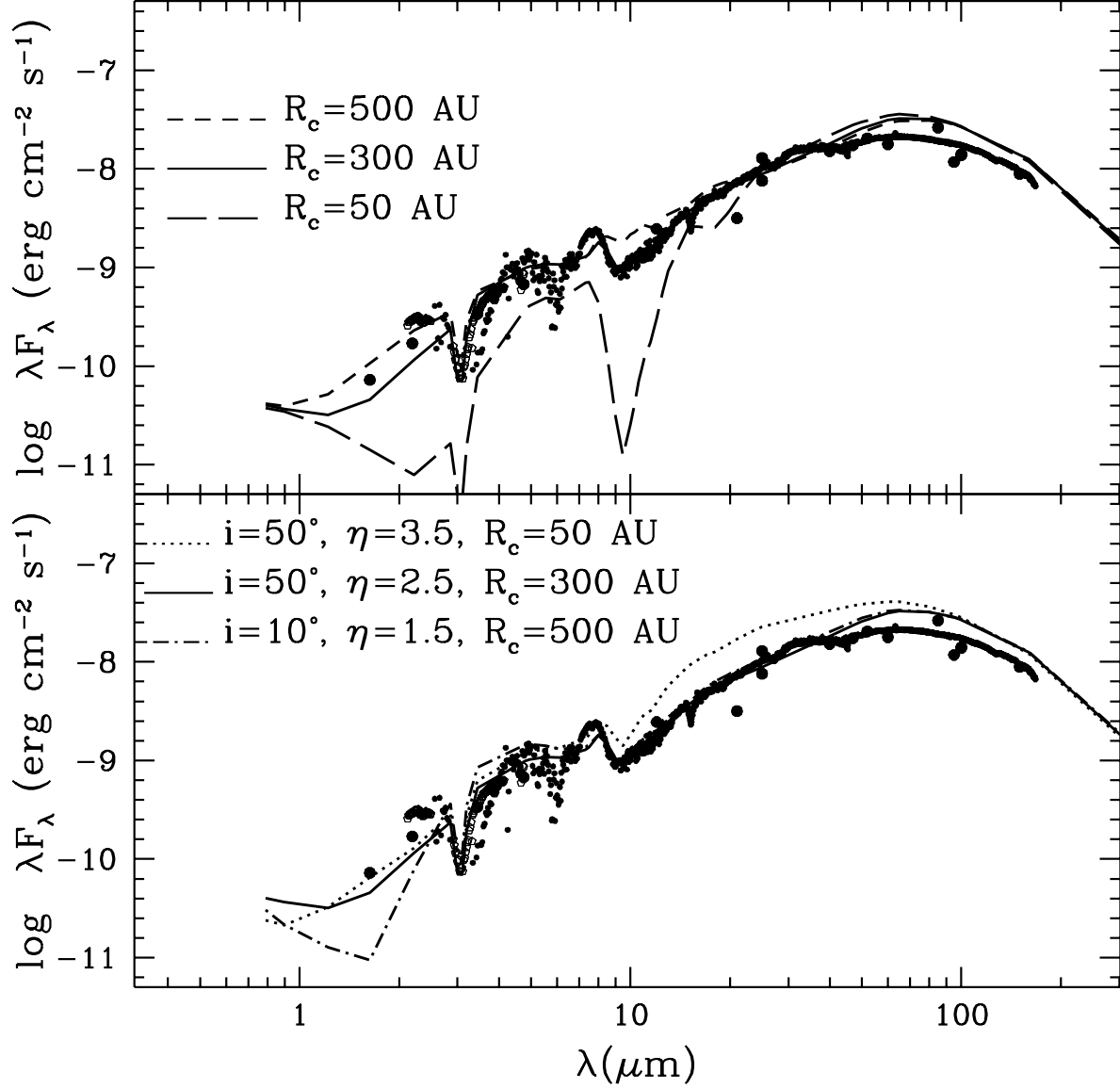


Fig. 5.— Upper: SED of the model with $L = 25L_{\odot}$, $\rho_1 = 4.5 \times 10^{-13} \text{ g cm}^{-3}$ and $\eta = 2.5$ for different centrifugal radii: 50 AU (long-dashed line), 300 AU (solid, the fiducial model) and 500 AU (short-dashed line). Observations as in Figure 3. Lower: Comparison of model SEDs for high η , low R_c (dotted) and low η , high R_c (dot-dashed line) at inclinations that provide the best fit to the observations. The fiducial model (solid) is shown for reference.

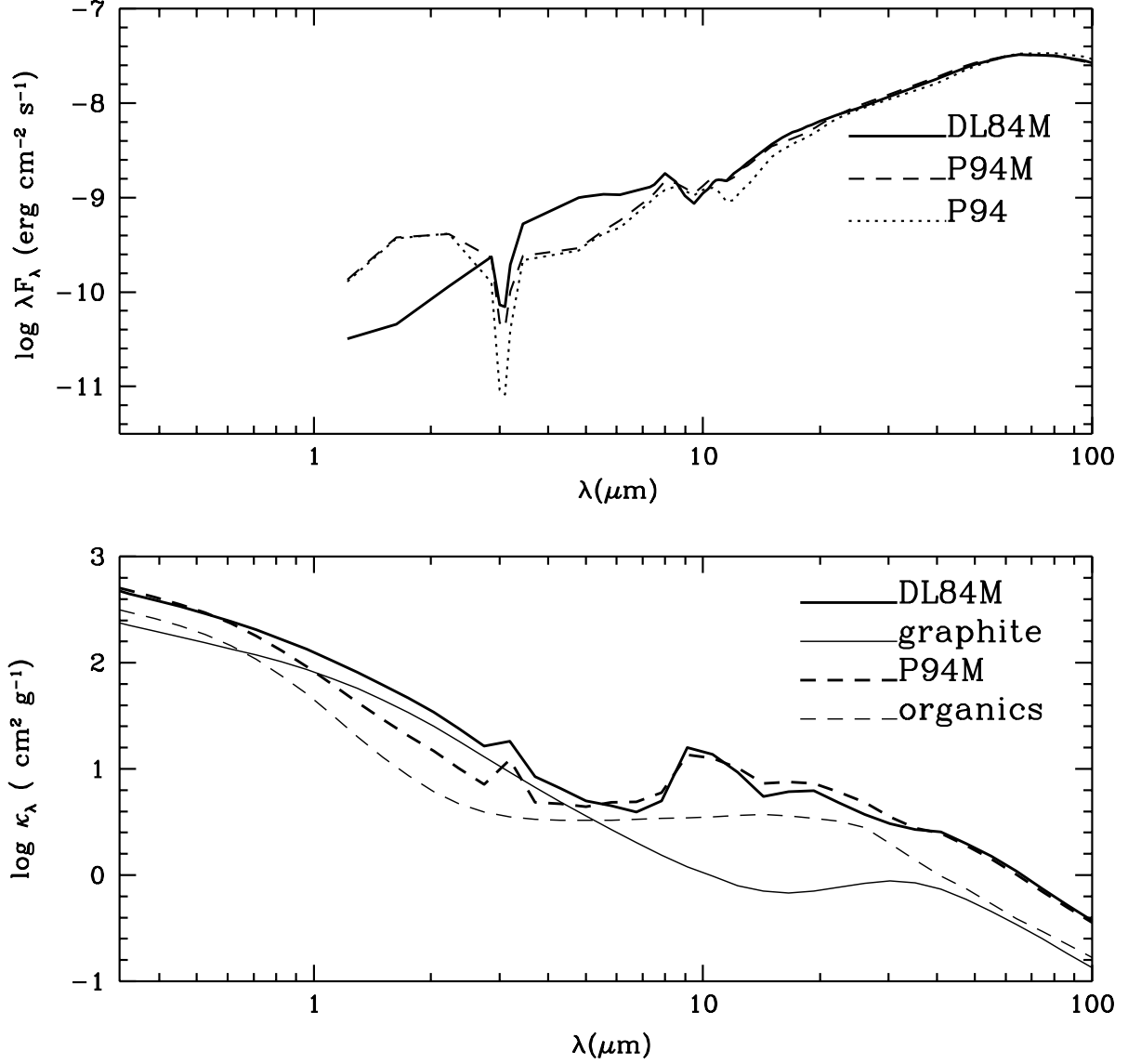


Fig. 6.— Upper: SED of the fiducial model with different dust mixtures. P94 (dotted line), P94M (dashed line), DL84M (solid line). Lower: total mass absorption coefficient from P94M (thick dashed line), organics (light dashed line), total mass absorption coefficient from DL84M (thick solid line), graphite (light solid line).

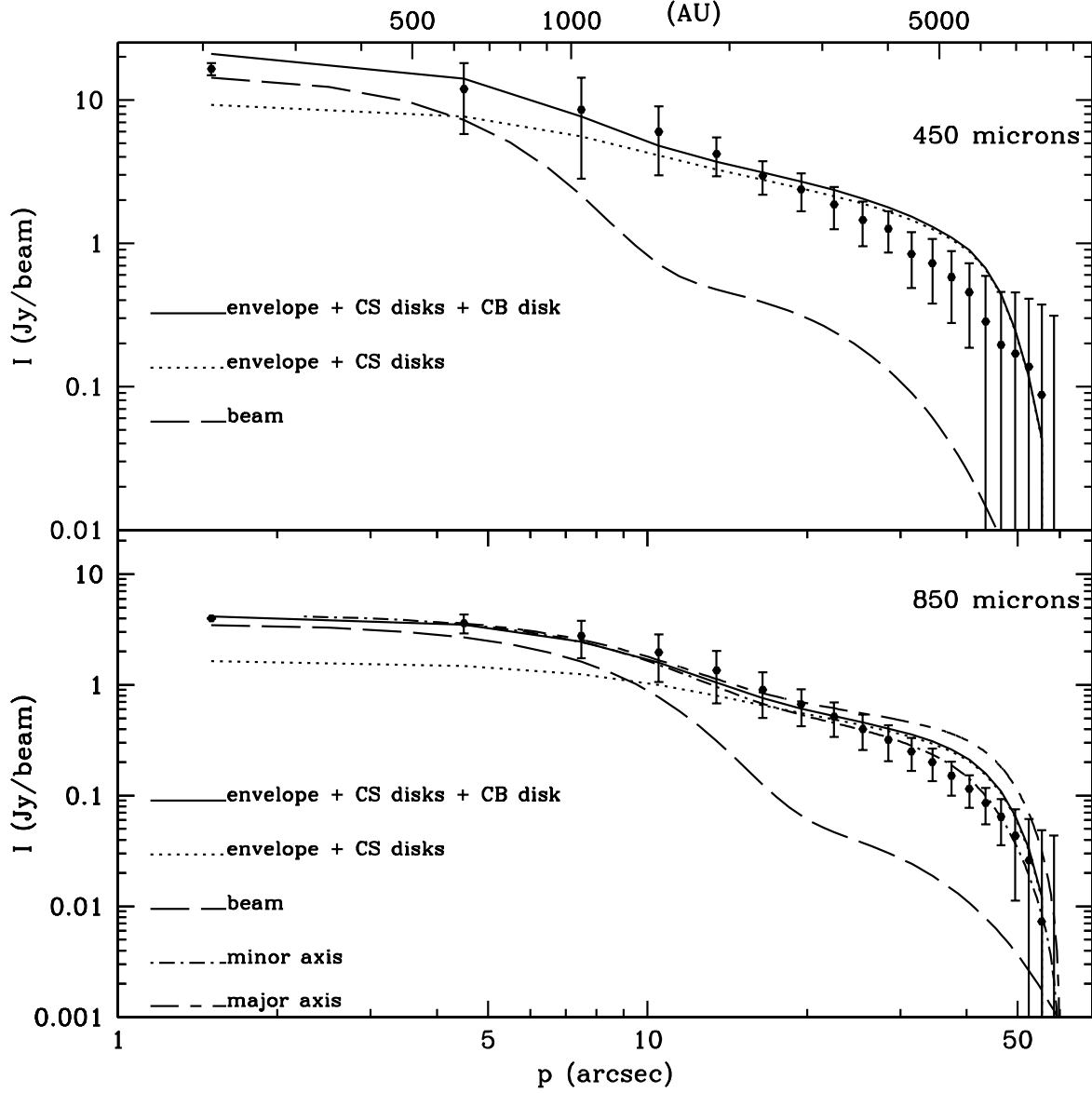


Fig. 7.— Spherically averaged spatial intensity profile at $450\mu m$ (upper panel) and $850\mu m$ (lower panel). SCUBA observations of Chandler & Richer 2000 (filled dots with error bars); predicted emission from the envelope (§5.1.1) plus circumstellar disks (CS, §5.3) (dotted line); predicted emission from the envelope, circumstellar disks, and circumbinary disk (CB, §5.4) (solid line). The predicted profile at $850\mu m$ along the minor axis (dot-dashed line) and the major axis (long-short dashed line) are also shown. The shape of the SCUBA beam is represented in each panel (long-dashed line).

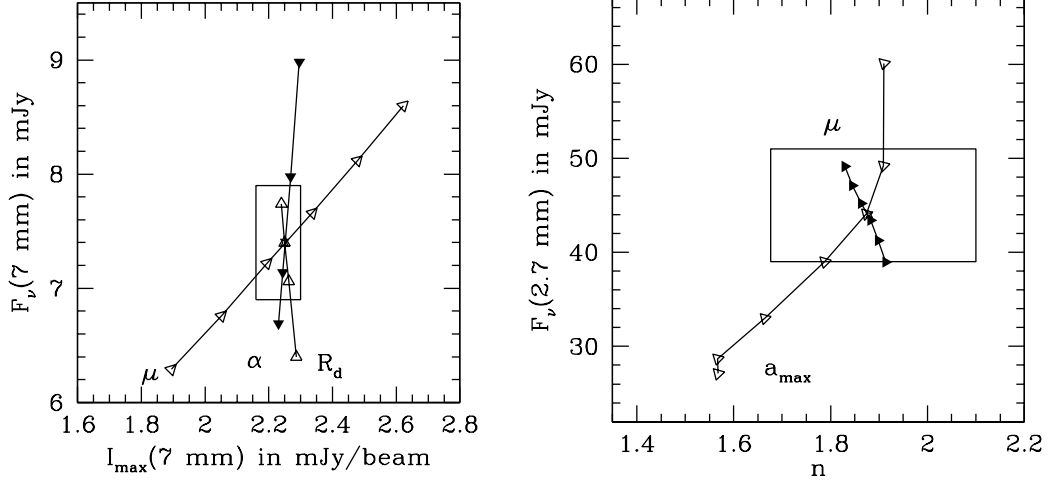


Fig. 8.— Dependence of observables on irradiated accretion disk parameters. Left panel: Flux vs maximum intensity at 7 mm as a function of inclination angle i (measured by $\mu = \cos i$), viscosity parameter α (or \sim disk mass) and disk radius R_d . Values plotted (increasing as indicated by the arrows) are $\mu = 0.4, 0.45, 0.5, 0.55, 0.6$ and 0.65 ; $\alpha = 0.0005, 0.001, 0.002$, and 0.003 , corresponding to masses, $M_d = 0.7, 0.4, 0.23$ and $0.16 M_\odot$, respectively; $R_d = 12, 13, 13.5$ and 14 AU. Right panel: Flux at 2.7 mm vs mm slope between 2.7 and 7 mm, as a function of inclination and a_{max} . Values of μ are the same as in the left panel, and $a_{\text{max}} = 10, 100, 200, 300, 400, 500$, and $600 \mu\text{m}$. The observation for the northern disk and its errors (taken from Rodríguez et al. 1998) are represented by a box.

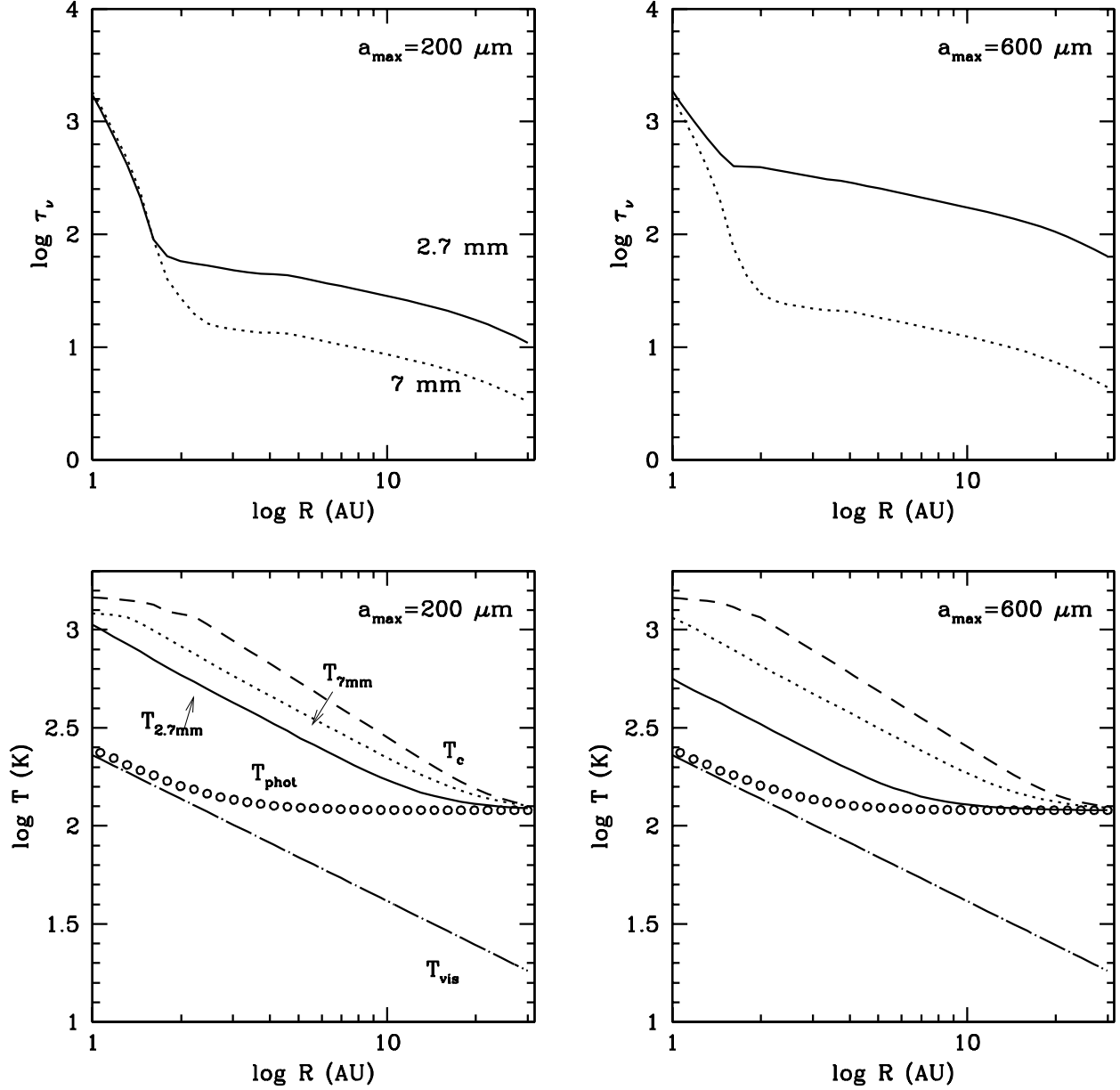


Fig. 9.— Properties of the circumstellar disks as a function of a_{\max} . Upper panels. Vertical optical depths as a function of radius for 2.7 mm (solid) and 7 mm (dotted). The value of a_{\max} is indicated in the panels. Lower panels. Characteristic temperatures as a function of radius: midplane temperature T_c (dashed line), photospheric temperature T_{phot} (circles). The temperatures of the height where the optical depth at a given wavelength (for a pole-on disk) becomes unity: 2.7 mm (solid) and 7 mm (dotted) are also shown. These correspond approximately to the brightness temperatures at those wavelengths (§5.3). Structural parameters other than a_{\max} as in Table 2.

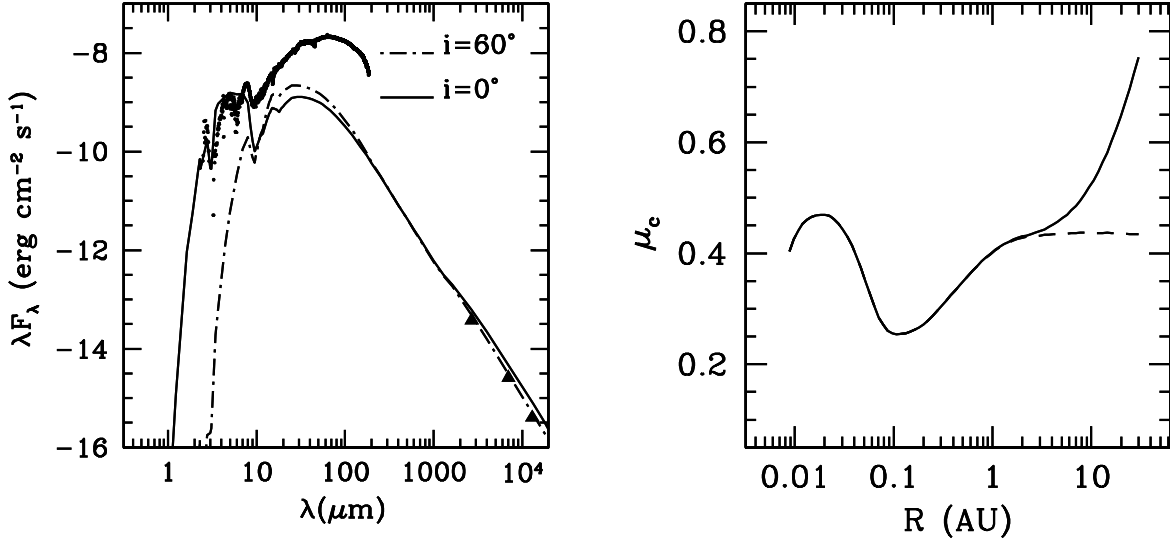


Fig. 10.— Left panel: SED for an irradiated disk model with parameters in Table 2, with an inclination angle $i = 0^\circ$ (solid line) and $i = 60^\circ$ (dotted-dashed line), showing the effect of self-occultation. Interferometric measurements of the northern disk (triangles; Rodríguez et al. 1998 and references therein) and the ISO data (dots) are also shown. Right panel: Cosine of the critical angle, μ_c , as a function of disk radius for radiation characteristic of the inner disk ($T \sim 4500$ K). For $\mu < \mu_c$, the outer disk absorbs the radiation of the inner disk. The dashed line is the purely viscous disk, the solid line is the disk irradiated by the envelope (§5.3).

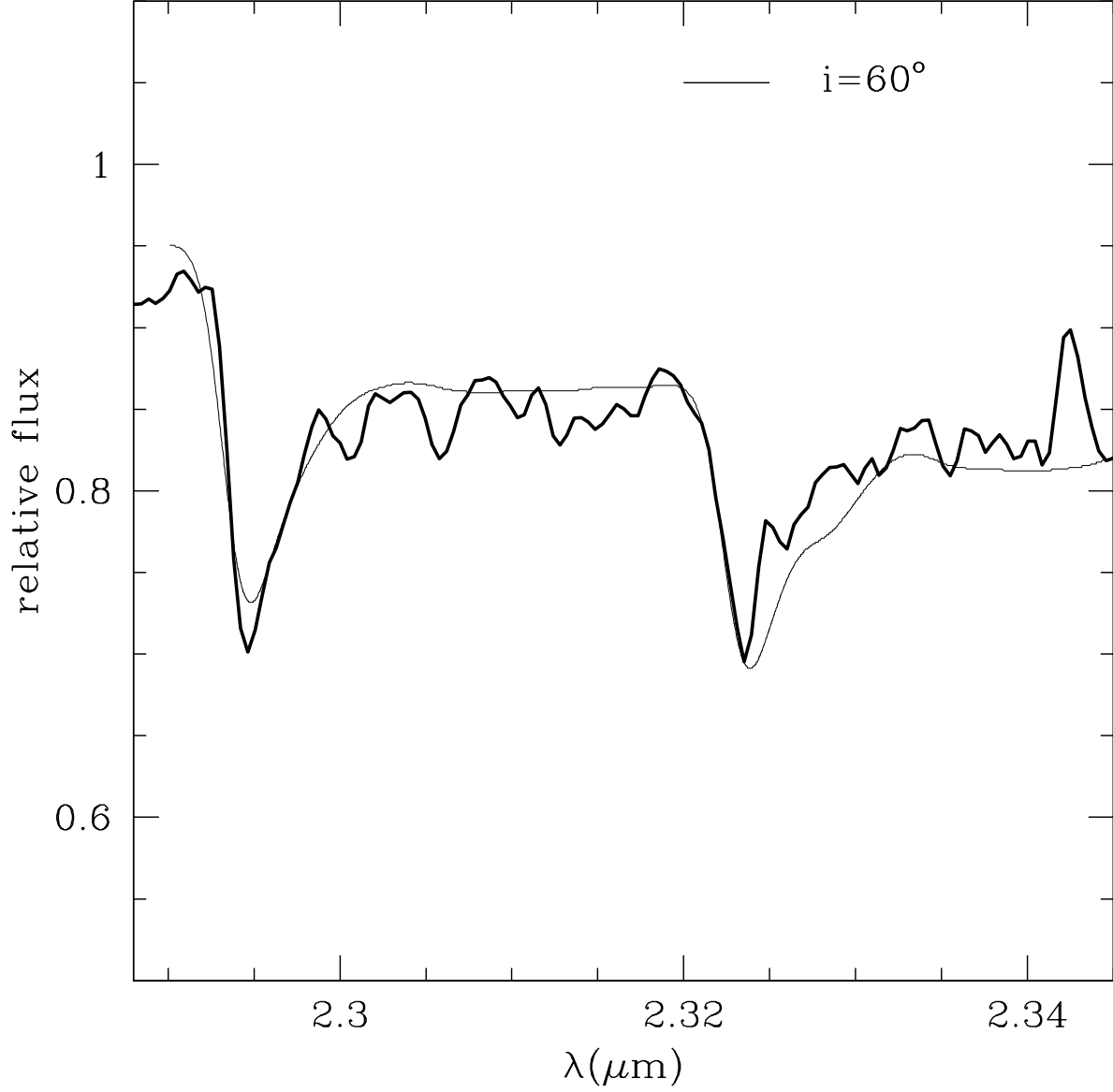


Fig. 11.— Portion of our SpeX spectrum of L1551 IRS 5 showing the first overtone bands of CO (heavy line). Calculations for a disk of mass accretion rate $2 \times 10^{-6} M_{\odot} \text{ yr}^{-1}$, stellar mass $0.3 M_{\odot}$ and stellar radius $1.4 R_{\odot}$, at an inclination angle of 60° (light line). The calculations have been convolved to a resolution of $R=2000$, and both observations and predictions have been normalized to the continuum.

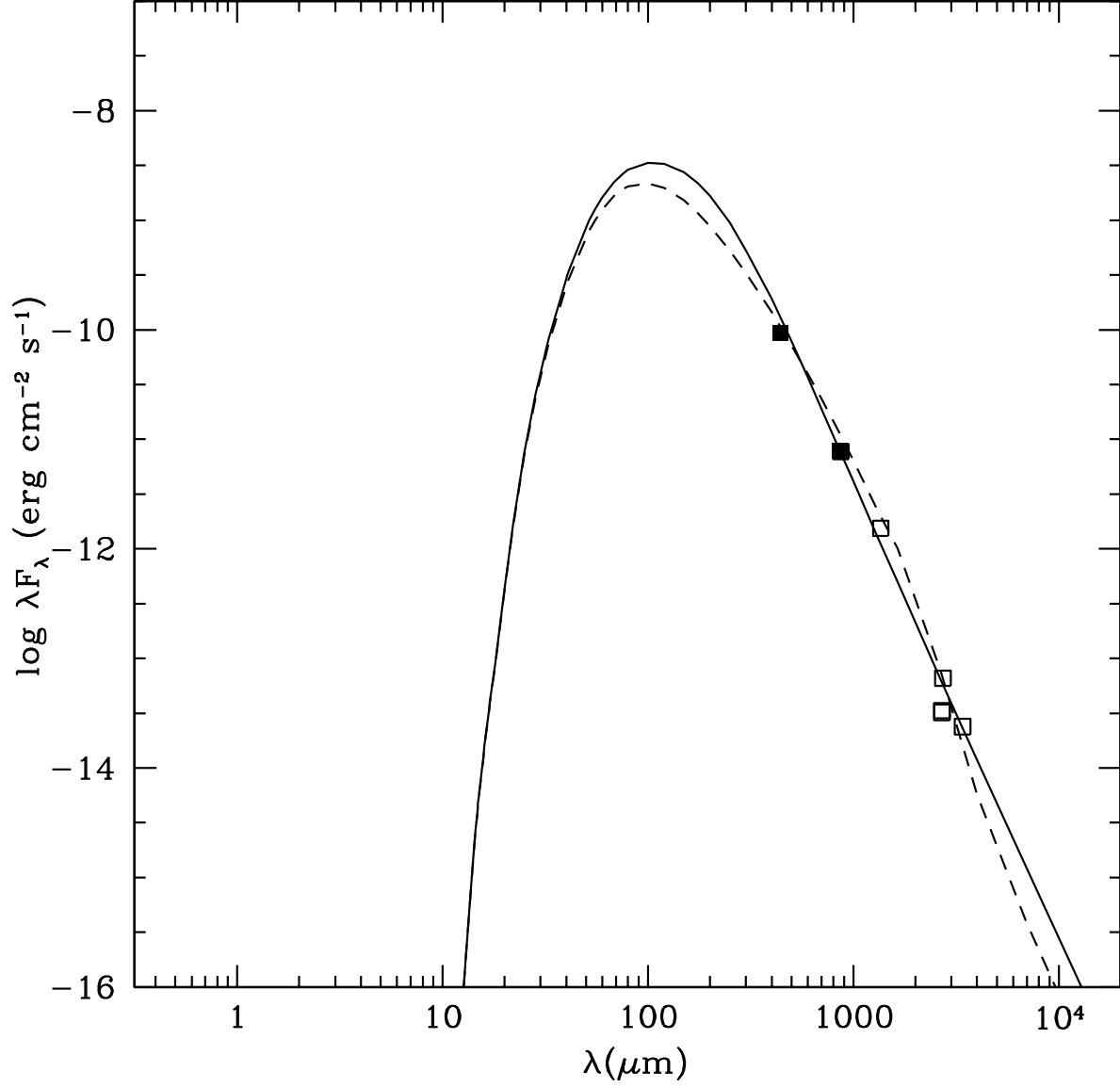


Fig. 12.— SEDs of the circumbinary disk obtained assuming a dust size distribution as in the envelope (solid line) or as in the circumstellar disks (dashed line). Fluxes at $450 \mu\text{m}$ and $850 \mu\text{m}$ (filled squares) come from the fit to the large-scale intensity distribution profiles, §5.2. Fluxes at other wavelengths are listed in Table 1 (open squares).

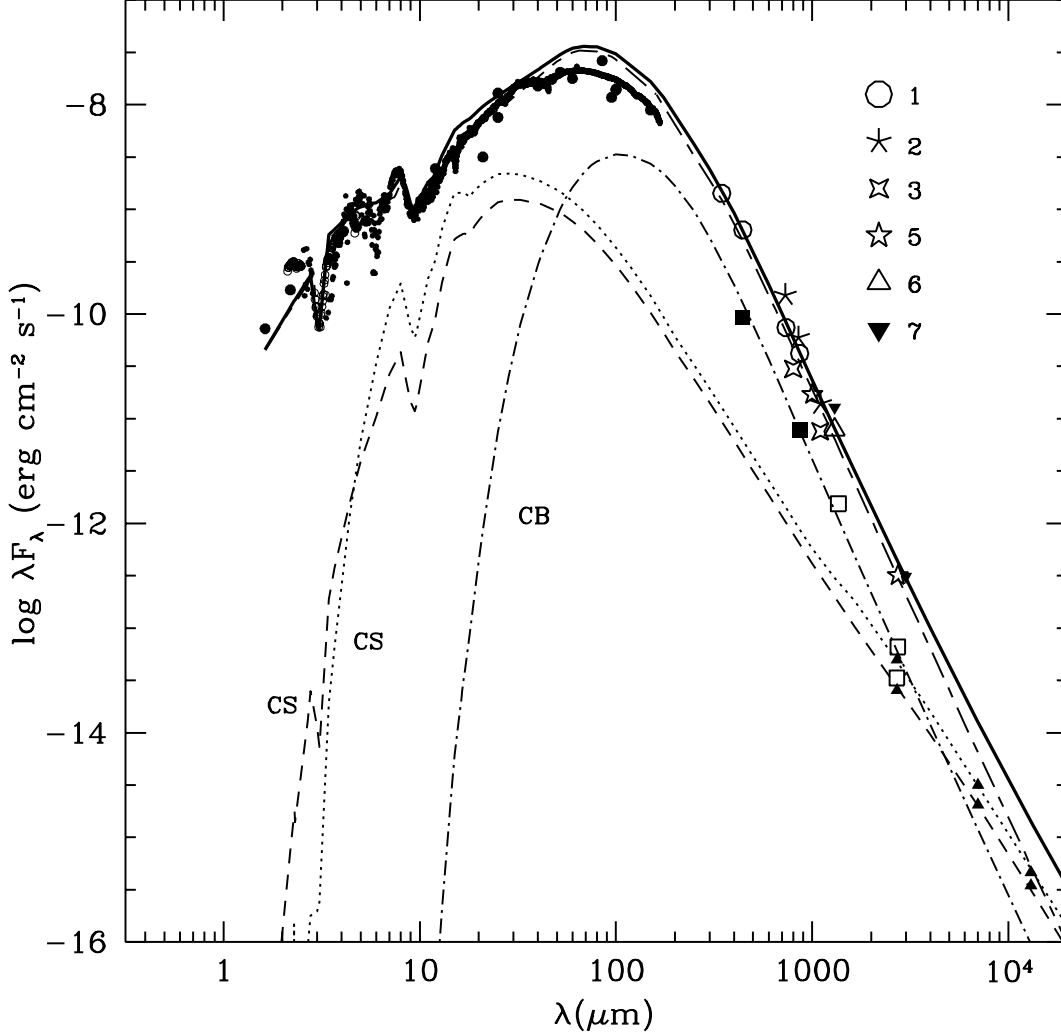


Fig. 13.— Composite SED (envelope + circumbinary disk + circumstellar disks) for a model with the parameters listed in Table 2 (solid line). Predicted SED of the envelope (short and long-dashed line). Predicted SEDs of the circumstellar disks (CS): Northern component (dotted line) and Southern component (dashed line). Predicted SED for a circumbinary disk (CB, dotted and dashed line). The IR observational data represented are from ISO (filled-small dots), SpeX (open-small dots), and photometry observations compiled by KCH93 (filled-big dots). Data for the circumstellar disks (filled triangles) and for the circumbinary disk (filled and open squares) and are the same as in Figures 10 and 12, respectively. For the remaining data points, the number from Table 1 reference list is indicated.